

FACULTY  
OF MATHEMATICS  
AND PHYSICS  
Charles University

1

BACHELOR THESIS

2

Martin Vavřík

3

**Simulation and Reconstruction  
of Charged Particle Trajectories  
in an Atypic Time Projection Chamber**

4

5

Institute of Particle and Nuclear Physics

6

Supervisor of the bachelor thesis: Mgr. Tomáš Sýkora, Ph.D.

7

Study programme: Physics

8

Prague 2025

- <sup>9</sup> I declare that I carried out this bachelor thesis independently, and only with the  
<sup>10</sup> cited sources, literature and other professional sources. It has not been used to  
<sup>11</sup> obtain another or the same degree.
- <sup>12</sup> I understand that my work relates to the rights and obligations under the Act  
<sup>13</sup> No. 121/2000 Sb., the Copyright Act, as amended, in particular the fact that the  
<sup>14</sup> Charles University has the right to conclude a license agreement on the use of this  
<sup>15</sup> work as a school work pursuant to Section 60 subsection 1 of the Copyright Act.

In ..... date .....  
Author's signature

<sup>16</sup> Dedication.

Title: Simulation and Reconstruction of Charged Particle Trajectories in an Atypical Time Projection Chamber **Added hyphen to avoid overfull hbox**

Author: Martin Vavřík

Institute: Institute of Particle and Nuclear Physics

Supervisor: Mgr. Tomáš Sýkora, Ph.D., Institute of Particle and Nuclear Physics

Abstract: Abstract.

Keywords: key words

# <sup>17</sup> Contents

<sup>18</sup>	<b>Motivation</b>	<sup>3</sup>
<sup>19</sup>	0.1 ATOMKI Anomaly . . . . .	<sup>3</sup>
<sup>20</sup>	0.1.1 ATOMKI Measurements . . . . .	<sup>3</sup>
<sup>21</sup>	0.1.2 Other Experiments . . . . .	<sup>4</sup>
<sup>22</sup>	0.2 X17 Project at IEAP CTU . . . . .	<sup>7</sup>
<sup>23</sup>	<b>1 Time Projection Chamber</b>	<sup>9</sup>
<sup>24</sup>	1.1 Charge transport in gases . . . . .	<sup>9</sup>
<sup>25</sup>	1.1.1 Drift . . . . .	<sup>10</sup>
<sup>26</sup>	1.1.2 Diffusion . . . . .	<sup>11</sup>
<sup>27</sup>	1.2 Examples of TPCs . . . . .	<sup>12</sup>
<sup>28</sup>	1.2.1 The original TPC at PEP-4 at SLAC . . . . .	<sup>12</sup>
<sup>29</sup>	1.2.2 The ALICE TPC . . . . .	<sup>12</sup>
<sup>30</sup>	1.2.3 The CERES/NA45 radial drift TPC . . . . .	<sup>12</sup>
<sup>31</sup>	1.3 Readout . . . . .	<sup>13</sup>
<sup>32</sup>	1.3.1 Multi-Wire Proportional Chamber . . . . .	<sup>13</sup>
<sup>33</sup>	1.3.2 Micro-Pattern Gaseous Detectors . . . . .	<sup>13</sup>
<sup>34</sup>	1.4 Orthogonal Fields TPC at IEAP CTU . . . . .	<sup>15</sup>
<sup>35</sup>	1.4.1 Motivation and Associated Challenges . . . . .	<sup>16</sup>
<sup>36</sup>	1.4.2 Coordinate Systems and Dimensions . . . . .	<sup>16</sup>
<sup>37</sup>	1.4.3 Magnetic Field Simulation . . . . .	<sup>18</sup>
<sup>38</sup>	<b>2 Track Simulation</b>	<sup>22</sup>
<sup>39</sup>	2.1 Microscopic Simulation . . . . .	<sup>22</sup>
<sup>40</sup>	2.1.1 First testing track . . . . .	<sup>23</sup>
<sup>41</sup>	2.1.2 Grid-like testing sample . . . . .	<sup>23</sup>
<sup>42</sup>	2.2 Runge-Kutta Simulation . . . . .	<sup>23</sup>
<sup>43</sup>	2.2.1 Testing sample . . . . .	<sup>26</sup>
<sup>44</sup>	<b>3 Track Reconstruction</b>	<sup>28</sup>
<sup>45</sup>	3.1 Reconstruction Assuming Steady Drift . . . . .	<sup>28</sup>
<sup>46</sup>	3.2 Ionization Electron Map . . . . .	<sup>29</sup>
<sup>47</sup>	3.2.1 Gradient Descent Algorithm . . . . .	<sup>36</sup>
<sup>48</sup>	3.2.2 Interpolation on the Inverse Grid . . . . .	<sup>37</sup>
<sup>49</sup>	3.3 Discrete Reconstruction . . . . .	<sup>39</sup>
<sup>50</sup>	<b>4 Energy Reconstruction</b>	<sup>41</sup>
<sup>51</sup>	4.1 Cubic Spline Fit . . . . .	<sup>41</sup>
<sup>52</sup>	4.2 Circle and Lines Fit . . . . .	<sup>43</sup>
<sup>53</sup>	4.2.1 Two-dimensional fit . . . . .	<sup>44</sup>
<sup>54</sup>	4.2.2 Three-dimensional fit . . . . .	<sup>45</sup>
<sup>55</sup>	4.2.3 Testing on a Runge-Kutta sample . . . . .	<sup>48</sup>
<sup>56</sup>	4.3 Runge-Kutta Fit . . . . .	<sup>48</sup>
<sup>57</sup>	4.3.1 Testing on a microscopic sample . . . . .	<sup>51</sup>
<sup>58</sup>	<b>Conclusion</b>	<sup>52</sup>

59	Bibliography	56
60	List of Abbreviations	64

# 61 Motivation

62 Or chapter 1? MFF UK thesis template uses Introduction as an unnumbered  
63 chapter, but it's not clear how they handle numbering inside the chapter. A Time  
64 Projection Chamber (TPC) [refs] is a gaseous detector that reconstructs charged  
65 particle trajectories by measuring the positions and drift times of ionization elec-  
66 trons (and sometimes also ions) created in the gas. The energies of these particles  
67 can be inferred from the curvatures of their trajectories in a magnetic field.

68 The goal of this thesis is to develop an algorithm for the reconstruction of  
69 charged particle trajectories and energy in an *atypic* TPC with orthogonal elec-  
70 tric and magnetic fields, hereafter referred to as the Orthogonal Fields TPC  
71 (OFTPC), used in the X17 project at the Institute of Experimental and Ap-  
72 plied Physics, Czech Technical University in Prague (IEAP CTU). Furthermore,  
73 we present the results of testing of several (gradually improving) developed algo-  
74 rithms with different samples of simulated data. Put this somewhere, (maybe just  
75 the abstract?). We use the Garfield++ toolkit [1] for simulations in combination  
76 with the ROOT framework [2] for data analysis and visualization. Some of our  
77 more demanding simulations are run on the MetaCentrum grid [3].

78 The X17 project in IEAP CTU aims to reproduce measurements of anomalous  
79 behavior in the angular correlation distribution of pairs produced by the Internal  
80 Pair Creation (IPC) mechanism [4] during the decay of certain excited nuclei  
81 ( $^{8}\text{Be}$ ,  $^{12}\text{C}$ , and  $^{4}\text{He}$ ) observed by a team at ATOMKI in Hungary. I would leave  
82 this here as a short summary before I explain it in more detail in the sections  
83 below.

84 Add citations: X17 project, VdG. Maybe also TPC, etc.

## 85 0.1 ATOMKI Anomaly

86 Many different theories propose the existence of *new light boson(s)* that are weakly  
87 coupled to ordinary matter [5]. These particles are potential dark matter candi-  
88 dates and could contribute to a solution of other issues with the Standard Model,  
89 such as the strong CP problem<sup>1</sup> and the anomalous muon magnetic moment. Mass  
90 range of axions?

91 A possible way of detecting such bosons with a short lifetime is to observe  
92 nuclear transitions of excited nuclei. If a boson was emitted during the transition  
93 and subsequently decayed into an electron-positron pair, we could observe this as  
94 a peak on top of the standard  $e^+e^-$  (both cursive and upright forms are used in  
95 different articles) angular correlation from the Internal Pair Creation (IPC) and  
96 the External Pair Creation (EPC).

### 97 0.1.1 ATOMKI Measurements

98 Historically, there were several measurements of the IPC in nuclear transitions  
99 in  $^{8}\text{Be}$  at Institute für Kernphysik (Frankfurt) [6, 7, 8] and at ATOMKI (Debre-  
100 cen, Hungary) [9, 10] resulting in different anomalies with invariant mass in the

---

<sup>1</sup>The CP symmetry could be violated in strong interactions according to the current formulation of quantum chromodynamics, but no such violation is observed.

range 5 – 15 MeV. This motivated the development of a better spectrometer at ATOMKI.

In 2015, a group at ATOMKI observed an anomalous IPC in  ${}^8\text{Be}$  [11]. They used the  ${}^7\text{Li}(p, \gamma){}^8\text{Be}$  reaction at the  $E_p = 1030$  keV proton capture resonance to prepare the 18.15 MeV excited state ( $J^\pi = 1^+$ ,  $T = 0$ ). This state decays predominantly through M1 transitions to the ground state ( $J^\pi = 0^+$ ,  $T = 0$ ) and to the 3.03 MeV state ( $J^\pi = 2^+$ ,  $T = 0$ ) [12]. **Transition figure – all transitions of isotopes? IPC figure?**

The angular correlation of the  $e^+e^-$  pairs created internally in these transitions were measured and compared to the simulation; results from a narrow  $E_{\text{sum}} = 18$  MeV region are shown in Fig. 0.1a. The simulation includes boson decay pairs for different boson masses. The disparity parameter  $y$  is used to describe the asymmetry of energy between the two particles. It is defined as

$$y = \frac{E_{e^-} - E_{e^+}}{E_{e^-} + E_{e^+}}, \quad (0.1)$$

where  $E_{e^-}$  and  $E_{e^+}$  are the kinetic energies of the electron and positron.

Their experimental setup was later upgraded (**details?**) and used for new measurements. In 2022 the  ${}^8\text{Be}$  anomaly was also measured using the  $E_p = 441$  keV resonance to produce the 17.64 MeV excited state ( $J^\pi = 1^+$ ,  $T = 1$ ) which again decays primarily to the ground state and the 3.03 MeV state [12]. The anomaly was also verified for  $E_p = 650$  and 800 keV where E1 transitions from the direct proton capture dominate [13]. The results for  $e^+e^-$  with  $E_{\text{sum}} \in [13.5, 20]$  MeV are shown in Fig. 0.1b.

The newer setup was also used in 2021 to study the  ${}^3\text{H}(p, e^+e^-){}^4\text{He}$  reaction at  $E_p = 510, 610$  and 900 keV [14], inducing direct and resonant capture populating the overlapping first 20.21 MeV ( $J^\pi = 0^+$ ) and second 21.01 MeV ( $J^\pi = 0^-$ ) excited states [15]. The comparison of simulated and measured  $e^+e^-$  pair angular correlations in the  $E_{\text{sum}} \in [18, 22]$  MeV region is shown in Fig. 0.1c.

In 2022, another anomaly was measured in the  ${}^{11}\text{B}(p, e^+e^-){}^{12}\text{C}$  process [16]. The  $E_p = 1388$  keV resonance was used to populate the 17.23 MeV excited state ( $J^\pi = 1^-, T = 1$ ) with a large width  $\Gamma = 1.15$  MeV [17]. This state decays mainly through E1 transitions to the ground state  $J^\pi = 0^+$  and to the 4.44 MeV state  $J^\pi = 2^+$ . To compensate for energy losses in the target, five energies in the range  $E_p = 1.5\text{--}2.5$  MeV were used. The experimental angular correlation for the 17.23 MeV transition to the ground state is shown in Fig. 0.1d.

Possible explanations of the anomaly include experimental effects, higher order processes in the Standard Model [18, 19] or even a protophobic fifth force mediated by a new 17 MeV boson X17 [20]. **Not sure if the introduction should be referenced since even though it is related, it is an independent theory developed only (?) to explain these measurements. Zhang and Miller: <https://www.sciencedirect.com/science/article/pii/S0370269321000010>**

### 0.1.2 Other Experiments

Since the ATOMKI measurements, several experiments have been initiated to attempt to replicate the results and search for the hypothetical X17 particle. The following experiments have already produced results. **Could cite the ATOMKI review paper here.**

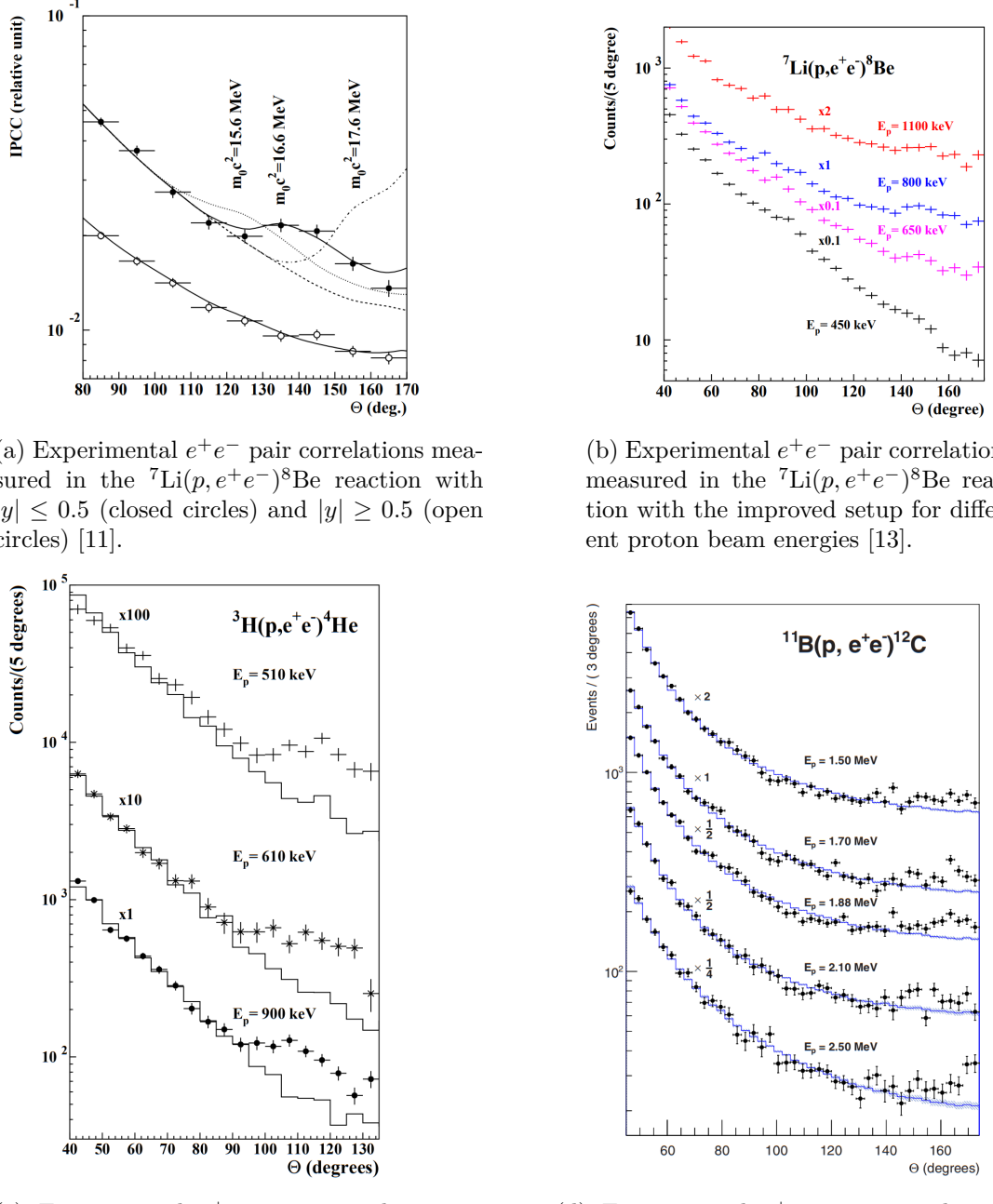


Figure 0.1: The ATOMKI anomalous IPC measured for different nuclei.



Figure 0.2: Results from the Hanoi spectrometer – angular  $e^+e^-$  pair correlations measured in the  ${}^7\text{Li}(p, e^+e^-){}^8\text{Be}$  reaction at  $E_p = 1225$  keV [21].

#### 145 Two-arm $e^+e^-$ spectrometer in Hanoi

146 The anomaly in  ${}^8\text{Be}$  has been observed with a high ( $> 4\sigma$  That's all they write  
147 in their article.) confidence by a team at the Hanoi University of Sciences for  
148  $E_p = 1225$  keV [21]. They built a two-arm spectrometer in collaboration with  
149 ATOMKI and calibrated it using the 17.6 MeV M1 transition. The results are  
150 shown in Fig. 0.2.

#### 151 Collisions at Nuclotron in Dubna

152 At the Joint Institute for Nuclear Research in Dubna, signal in the form of en-  
153 hanced structures in the  $\gamma\gamma$  spectra at  $\sim 17$  and  $\sim 38$  MeV invariant masses for  
154  $p + \text{C}$ ,  $d + \text{C}$  and  $d + \text{Cu}$  reactions at momenta 5.5, 2.75, and 3.83 GeV per nu-  
155 cleon [22]. Monte Carlo simulations support the conclusion that the signals are  
156 a consequence of a decay of unknown particles X17 and E38.

#### 157 The MEG II (Muon Electron Gamma) experiment

158 Experiments using the  ${}^7\text{Li}(p, e^+e^-){}^8\text{Be}$  reaction were carried out at the Paul  
159 Scherrer Institute with the MEG II superconducting solenoid spectrometer [23].  
160 Analysis of the data with  $E_p = 1080$  keV exciting both of the resonances (beam  
161 fully stopping in the target) found no significant evidence supporting the X17  
162 hypothesis, results are shown in Fig. 0.3. An upper bound (at 90% confidence)  
163 on the X17-to- $\gamma$  branching ratio was set at  $1.2 \cdot 10^{-5}$  for the 18.15 MeV state  
164 (larger than the ratio  $5.8 \cdot 10^{-6}$  obtained by ATOMKI in 2016). Could add their  
165 90% C.L bounds figure also. Insufficient statistics – 6.2 % ( $1.5\sigma$ ) p-value.

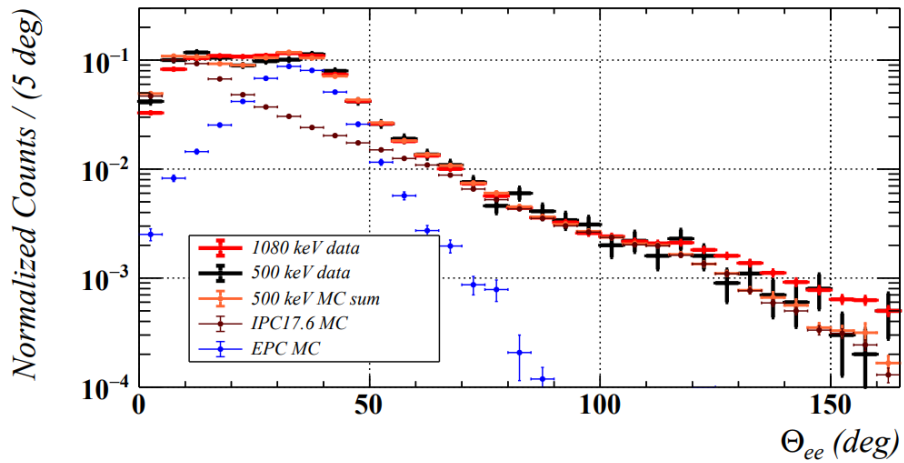


Figure 0.3: Results from the MEG II experiments – angular correlation of  $e^+e^-$  pairs with  $E_{\text{sum}} \in [16, 20]$  MeV measured in the  ${}^7\text{Li}(p, e^+e^-){}^8\text{Be}$  reaction with proton beam energies 500 and 1080 keV. The 500 keV dataset is fitted with Monte Carlo of both the IPC deexcitation and the EPC produced by gammas [23].

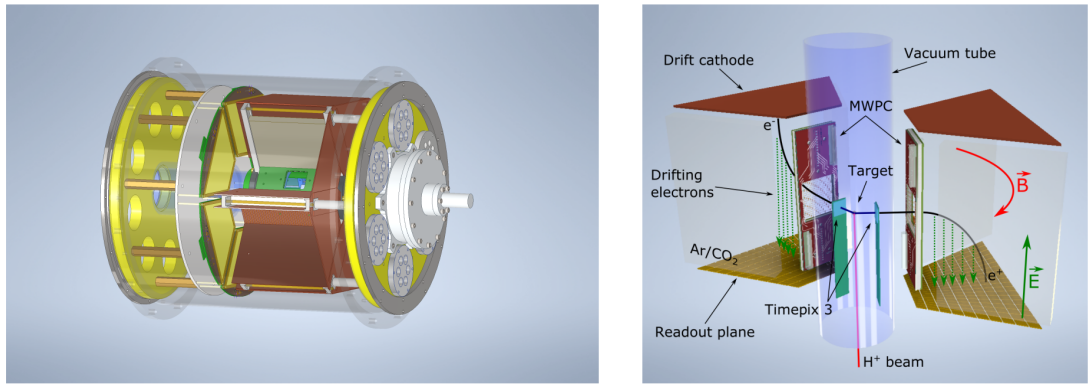


Figure 0.4: Schematics of the detector at the Van der Graaff facility at IEAP CTU (ref.).

## 166 0.2 X17 Project at IEAP CTU

167 The aim of the X17 project at the Van der Graaff facility of the Institute of  
 168 Experimental and Applied Physics, Czech Technical University in Prague is to  
 169 reproduce the results of the original ATOMKI experiments with  ${}^7\text{Li}$  and  ${}^3\text{H}$  tar-  
 170 gets using an independent  $e^+e^-$  spectrometer. In order to effectively measure the  
 171 anomaly, we need to reconstruct both the energy and the angular correlation of  
 172 the  $e^+e^-$  pairs. The spectrometer will use three layers of detectors to achieve this  
 173 – Timepix3 (TPX3) silicon pixel detector and Multi-Wire Proportional Cham-  
 174 ber (MWPC) layers for the angle reconstruction and a Time Projection Cham-  
 175 ber (TPC) layer for the energy reconstruction. The schematics of the prepared  
 176 detector is in Fig. 0.4 Spectrometer CAD drawing (coordinates here or next chap-  
 177 ter?). Cite some VdG paper, mention grant? Using [https://cernbox.cern.ch/pdf-viewer/public/rf0oU1nqVLN3acZ/LuzH\\_submitted.pdf](https://cernbox.cern.ch/pdf-viewer/public/rf0oU1nqVLN3acZ/LuzH_submitted.pdf).

178  
 179 The energy of  $e^+e^-$  pair produced in the reaction is given by the energy

available  $E_r$  in the reaction and can be distributed between them arbitrarily. Nonetheless in the decay of the hypothetical X17 particle, electron and positron should have similar energy and we can therefore use a cut  $|y| \leq 0.5$  in the disparity parameter (defined in Equation 0.1 **it was already used in ATOMKI figure captions, that's why it is defined prior to this**). Interesting events should rarely have a particle with an energy below  $E_r/4$  (roughly 4 MeV). Electrons with such low energies are scattered significantly by even a thin layer of relatively light material, for this reason the TPX3 layer will be inside of the vacuum tube and the tube will have a thinned aluminum segment or Kapton<sup>TM</sup> windows.

TPX3 can measure (in each  $55 \times 55 \mu\text{m}$  pixel of its  $256 \times 256$  grid) time-of-arrival (ToA) with 1.6 ns precision and time-over-threshold (ToT) which reflects the deposited energy. This potentially allows 3D tracking if we increase the chip thickness at the cost of increased scattering. The layer can reconstruct the reaction vertex and the angular correlation with high precision.

The layer of MWPCs with sensitive area  $40 \times 38 \text{ mm}^2$  will be outside of the beam pipe. It will provide an extra point on the particle trajectory which can help with the estimation of the reaction vertex and improve the TPC performance by providing its entry point.

The TPCs that are the subject of this thesis, are in a magnetic field generated by permanent magnets positioned between them and provide 3D track reconstruction and subsequent momentum and particle identification (its charge, or even type based on its stopping power). They avoid radiative losses thanks to the low density and atomic number of the gas mixture. For the readout, triple Gas Electron Multiplier (GEM) will be used. The magnetic field layout in our TPCs is atypical – orthogonal to the electric field inside the chamber, this is why we call them Orthogonal Fields TPC (OFTPC). Further details about our OFTPCs are provided in section 1.4.

# 1. Time Projection Chamber

A Time Projection Chamber (TPC) is a gaseous detector that uses the drift times of ionization electrons produced by a charged particle in an (ideally uniform) electric field to reconstruct the particle's 3D trajectory. The 2D projection is measured by an amplification stage at the end of the drift volume. When placed inside a magnetic field (typically parallel to the electric field), the momentum of the incident particle can be inferred from the curvature of its trajectory. Particle identification is also possible using the ionization energy loss inside the TPC (see Fig. 1.1). The following text (including Sections 1.1 and 1.3) is based primarily on the reviews by Hilke [24] and the Particle Data Group [25].

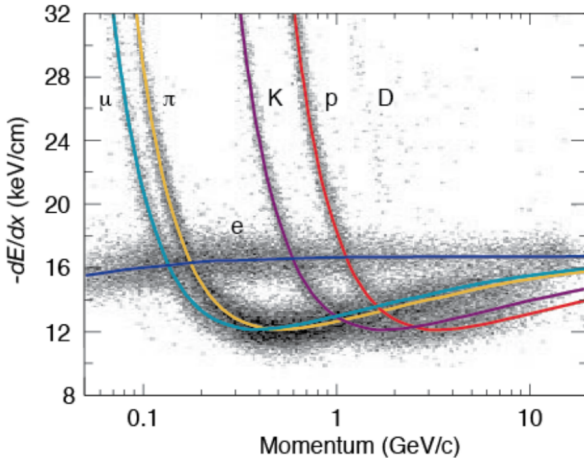


Figure 1.1: Particle identification in the PEP-4 TPC at SLAC based on the energy loss per distance  $\frac{dE}{dx}$  in the 80:20 Ar:CH<sub>4</sub> filling at 8.5 atm pressure [26]. The reference doesn't point to the original PEP-4 article because this adapted version of the original picture that they used in the DUNE article looks better.

Large TPCs are sensitive to small distortions in the electric field (imperfections in the field cage, accumulation of positive ions in the gas volume) and to  $\mathbf{E} \times \mathbf{B}$  effects on the drift velocity (see Eq. (1.1) below). Diffusion of the drifting electrons deteriorates the spacial resolution significantly, but it can be reduced up to  $\sim 10$  times by a strong  $\mathbf{B} \parallel \mathbf{E}$  field (see Eq. (1.8)).

In neutrino and other rare-event experiments, large (up to 600 tons) Liquid Argon TPCs (LArTPCs) are used for particle identification and calorimetry. The ionization electrons can be drifted for many meters with a small diffusion. Scintillation photons are also measured. Negative ions?

## 1.1 Charge transport in gases

When a charged particle crosses the volume of a TPC, it loses energy by excitation and ionization of the detector gas (how much – from  $dE/dx +$  density → footnote?). Most ionizing collision produce a single ionization electron, sometimes a few secondary electrons are produced near the collision vertex, creating a cluster. In rare cases, the ionization electron has energy large enough to create

232 a measurable track, such an electron is called a  $\delta$ -electron (terminology, just like  
233 bellow – technically it's a (primary) ionization electron causing other (secondary)  
234 ionization).

235 After their release, the ionization electrons are separated from positive ions  
236 by the electric field and they both drift and diffuse in opposite directions towards  
237 the electrodes. The charges are accelerated (different word?) by the electric field  
238 inside the chamber, and they lose speed by colliding with the gas particles, quickly  
239 reaching a constant (for a given field  $\mathbf{E}, \mathbf{B}$ ) mean drift velocity. The electrons can  
240 be absorbed by electronegative impurities, such as halides,  $\text{O}_2$ , and  $\text{H}_2\text{O}$ .

241 In mixtures with a noble gas component, if the excitation energy of the noble  
242 gas is higher than the ionization potential of an admixture, more free electrons can  
243 be produced through collisions of the gas particles (so-called Penning transfer)  
244 and through absorption of emitted photons.

245 If the electric field is strong enough, the electrons can cause further ion-  
246 ization and excitation of the gas, leading to the development of a Townsend  
247 avalanche (ref).

### 248 1.1.1 Drift

249 In many gases (called "hot", e.g., Ar or  $\text{CH}_4$ ), the drift velocity is much greater  
250 than that of their thermal motion thanks to a high proportion of elastic collisions.  
251 On the other hand, "cold" gases like  $\text{CO}_2$  have a higher proportion of inelastic  
252 collisions (e.g., thanks to the excitation of rotational and vibrational states) and  
253 therefore much lower (value? magnitude (implied)?). Or maybe it  
254 is not so simple, because slowing down the electrons inelastically into a certain  
255 minimum of elastic scattering cross-section increases drift velocity? In case of  
256  $\text{Ar}+\text{CO}_2$  this is clearly not the case for low electric fields, so maybe irrelevant  
257 here (or is the effect opposite for small additions?).

258 The ions produced by the ionization lose a significant portion of their energy  
259 during each collision since their mass is close to the mass of the gas particles (see  
260 the source material – average energy loss during collision  $\Delta E = \frac{2m_i M}{(m_i + M)^2}$ , this  
261 way it's more accurate). This, together with their large collision cross section,  
262 makes their drift velocity much smaller (about three orders of magnitude) and  
263 their energy is close to thermal. Since their momenta are not randomized to such  
264 an extent during collisions, their diffusion is smaller (move this to the diffusion  
265 subsection, reformulate).

266 The drift is also influenced by the magnetic field. Langevin derived a good  
267 approximation for the drift velocity vector:

$$\mathbf{v}_d = \left( \frac{\mathbf{E}}{\|\mathbf{E}\|} + \omega\tau \frac{\mathbf{E} \times \mathbf{B}}{\|\mathbf{E}\| \|\mathbf{B}\|} + \omega^2\tau^2 \frac{\mathbf{E} \cdot \mathbf{B}}{\|\mathbf{E}\| \|\mathbf{B}\|} \cdot \frac{\mathbf{B}}{\|\mathbf{B}\|} \right) \frac{q\tau}{m(1 + \omega^2\tau^2)} \|\mathbf{E}\|, \quad (1.1)$$

268 where  $q$  is the charge of the particle,  $m$  is its mass,  $\tau$  is the mean time between  
269 collisions and  $\omega = \frac{q}{m} \|\mathbf{B}\|$  is the Larmor frequency. For orthogonal fields  $\mathbf{E} \perp \mathbf{B}$ ,  
270 it can be shown that the magnetic field bends the direction of the drift by the  
271 so-called Lorentz angle:

$$\tan \psi = -\omega\tau. \quad (1.2)$$

272 The drift of ions is only negligibly influenced by the magnetic field ( $\omega\tau \sim 10^{-4}$   
273 is small due to the low drift velocity – better (?) because it takes  $\tau$  into account

<sup>274</sup> and differs only by E/B ratio (if the magnetic contribution to the magnitude is  
<sup>275</sup> small)). In a standard TPC,  $\mathbf{E}$  is parallel to  $\mathbf{B}$  and the influence of the magnetic  
<sup>276</sup> field on the drift is minimal. Without magnetic field, we can write

$$\mathbf{v}_d = \frac{q\tau}{m} \mathbf{E} = \mu \mathbf{E}, \quad (1.3)$$

<sup>277</sup> where  $\mu$  is called charge mobility.

### <sup>278</sup> 1.1.2 Diffusion

<sup>279</sup> All of the theory is from the same source mentioned at the beginning. None of the  
<sup>280</sup> simulations explicitly depend on this. Due to collisions, a cloud of electrons or  
<sup>281</sup> ions originating from the same point will show a Gaussian density distribution at  
<sup>282</sup> time  $t$  while drifting in the electric field  $\mathbf{E} = (0, 0, E_z)$  along the  $z$ -coordinate (<sup>283</sup> coordinates defined by the electric field):

$$\rho(x, y, z, t) = (4\pi Dt)^{-\frac{3}{2}} \exp\left(-\frac{x^2 + y^2 + (z - v_d t)^2}{4Dt}\right), \quad (1.4)$$

<sup>284</sup> where the diffusion coefficient  $D$  can be expressed as

$$D = \frac{\lambda^2}{3\tau} = \frac{\lambda v_d}{3} = \frac{v_d^2 \tau}{3} = \frac{2\varepsilon\tau}{3m}, \quad (1.5)$$

<sup>285</sup> where  $\lambda$  is the mean free path and  $\varepsilon$  the mean kinetic energy. The lateral diffusion  
<sup>286</sup> width  $\sigma_x$  after a drift distance  $L$  can be expressed as

$$\sigma_x^2 = 2Dt = \frac{4\varepsilon L}{3qE_z}. \quad (1.6)$$

<sup>287</sup> The minimal diffusion width is given by the lowest possible energy of the particles  
<sup>288</sup>  $\varepsilon_{\text{th}} = \frac{3}{2}kT$  (corresponding to thermal motion):

$$\sigma_{x, \text{min}}^2 = \frac{2kTL}{qE}. \quad (1.7)$$

<sup>289</sup> For electrons in "cold gases" (e.g., Ar/CO<sub>2</sub> mixture), the diffusion approaches  
<sup>290</sup> this limit up to a certain field intensity (~100 V/cm at 1 atm pressure)<sup>1</sup>. In  
<sup>291</sup> reality, the transversal diffusion of electrons can differ significantly from their  
<sup>292</sup> longitudinal diffusion and simulations are necessary to get a precise result.

<sup>293</sup> In most TPCs, the transversal (but not the longitudinal) diffusion is reduced  
<sup>294</sup> by the magnetic field, since it is parallel to the electric field and curves the dif-  
<sup>295</sup> fusing electrons around their mean trajectory:

$$\frac{D_T(B)}{D_T(0)} = \frac{1}{C + \omega^2 \tau_2^2}, \quad (1.8)$$

<sup>296</sup> where  $C$  and  $\tau_2$  are parameters dependent on the gas used. At low intensity of  
<sup>297</sup> the magnetic field, we can use an approximation  $C \approx 1$  and  $\tau_2 \approx \tau$ .

---

<sup>1</sup>For us  $\sigma_{x, \text{min}} = 0.45$  mm, quite close to the actual diffusion 0.5-0.7 mm – details of the calculation.

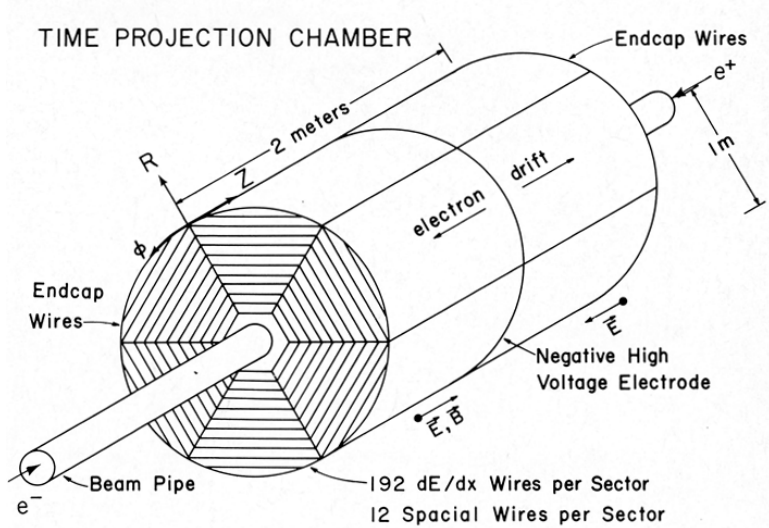


Figure 1.2: Schematic view of the PEP-4 TPC [27]. A charged particle produced in a collision in the beam pipe creates a spiral ionization track in the magnetic field. The central cathode then accelerates ionization electrons towards the endcap anode wires where they are multiplied and read out.

## 298 1.2 Examples of TPCs

### 299 1.2.1 The original TPC at PEP-4 at SLAC

300 The original TPC used in the PEP-4 experiment at SLAC in the 1980s (Fig. 1.2)  
 301 was a  $2 \times 2$  m cylinder with a central cathode that produced a strong electric field,  
 302 making the ionization electrons drift towards one of the endcaps. The readout  
 303 consisted of MWPCs, where electrons are accelerated towards the anode wires  
 304 fast enough to further ionize the gas and cause an avalanche.

### 305 1.2.2 The ALICE TPC

### 306 1.2.3 The CERES/NA45 radial drift TPC

307 CERES/NA45 – very inhomogeneous magnetic field. They used look-up tables for  
 308 reconstruction, which they calculated by integrating the Langevin drift velocity  
 309 equation with Runge-Kutta.

310 From [28]:

311 10.2 Coordinate transformation The detector specific hit coordinates (pad, time,  
 312 plane) are transformed to spatial coordinates ( $x, y, z$ ) via look-up tables. The  
 313 transformation contains the information about the transport process of the charged  
 314 clusters in the electric and magnetic fields inside the TPC. The look-up tables  
 315 are calculated using a Runge-Kutta method [39] that calculates the drift trajec-  
 316 tory using in each point the drift velocity vector (Eq. 3), starting at the cathode  
 317 plane. The drift between the cathode plane and the pad plane is absorbed in a  
 318  $\varphi$ -dependent time offset due the fact that each Front-End Electronic (FEE) chan-  
 319 nel had a slightly different capacitance. The difference between the MAGBOLTZ  
 320 Monte Carlo drift [19] and the actual drift velocity vector is accounted for with a

321 z- and r(E)-dependent correction for the drift velocity component parallel to the  
322 electric field and the one parallel to  $E \times B$

## 323 1.3 Readout

### 324 1.3.1 Multi-Wire Proportional Chamber

325 In most TPCs operated in experiments, Multi-Wire Proportional Chamber (MWPC)¶  
326 was used for the readout. The electrons enter the chamber through a cathode  
327 grid and get accelerated by a strong electric field towards the parallel, thin an-  
328 ode wires and create an avalanche, multiplying the signal. The trajectory can be  
329 reconstructed from the drift time and two coordinates measured using  
330 a) two segmented cathodes (wires or strips) rotated by 90° or  
331 b) the ratio of charge collected on two sides of the hit resistive wires.  
332 For high counting rates, the positive ions from the avalanches accumulate, cre-  
333 ating a space charge that distorts the electric field. This can be solved by using  
334 a gating grid near the readout plane to collect these ions at the cost of introducing  
335 a dead time in the detector. [Add some figure.](#)

### 336 1.3.2 Micro-Pattern Gaseous Detectors

337 In order to avoid MWPC limitations (e.g., diffusion, wire  $E \times B$  effect, space  
338 charge effects), a family of Micro-Pattern Gaseous Detector (MPGD) technologies  
339 are being developed. The readouts can reach higher spatial resolution (down to  
340 30 µm) with faster response time (ns range) and much higher rate capability.

#### 341 Gas Electron Multiplier

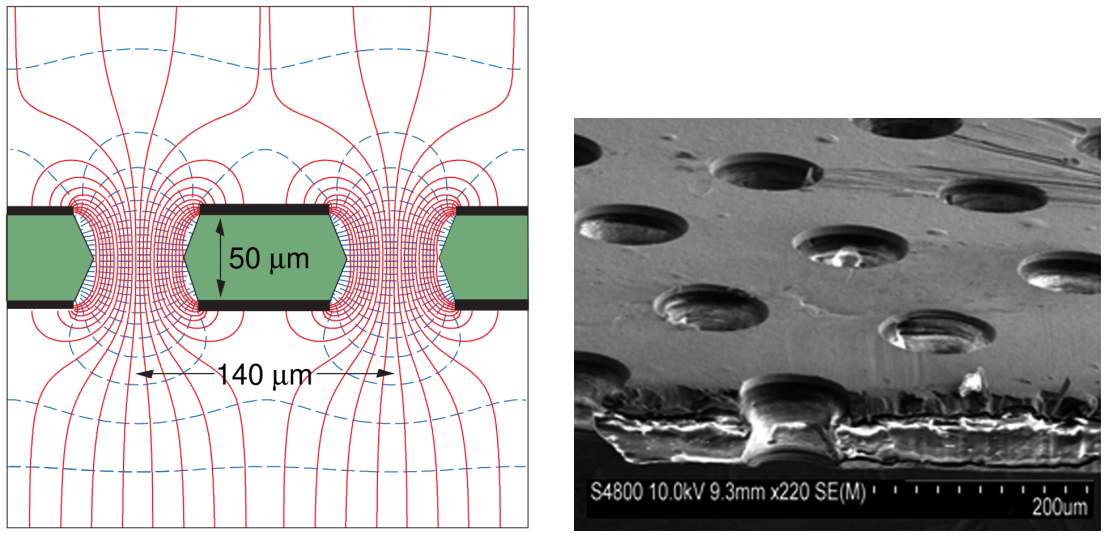
342 A Gas Electron Multiplier (GEM) is a thin metal-coated polyimide sheet with  
343 a dense pattern of small, chemically etched holes (Fig. 1.3). The amplification  
344 is achieved by applying voltage across the metal layers and placing the foil be-  
345 tween two moderate uniform electric fields. This creates a strong electric field  
346 inside the holes that accelerates the incoming electrons and causes avalanches  
347 (see Fig. 1.4). Some charges may land on the dielectric surfaces due to diffusion,  
348 modifying the field and affecting gain.

349 Double or triple stacks of GEMs are usually used to create a sufficient gain  
350 while maintaining stability (reducing discharges). From the last foil, the electrons  
351 drift to a segmented anode where the signal is read. The ion backflow is reduced  
352 compared to MWPC.

353 A cheaper alternative (especially for large area coverage) is a THick GEM  
354 (THGEM) with a ~10-fold upscaling of geometrical parameters. It can be made  
355 by mechanically drilling holes into a standard Printed Circuit Board (PCB) and  
356 creating a circular rim around the holes by etching the metal coating.

#### 357 Micromegas

358 In a MICRO-MEsh GAseous Structure (Micromegas) ([in sources I viewed it is not](#)  
359 [capitalized](#)) electrons pass through a fine mesh (made out of very thin wires) into  
360 a narrow amplification gap where they are multiplied in the high field and read



(a) A schematic view of a GEM cell with its typical dimensions, electric field lines (red), and equipotentials (blue) [25].

(b) A scanning electron microscope image of a GEM foil [29].

Figure 1.3: Gas Electron Multiplier (GEM).

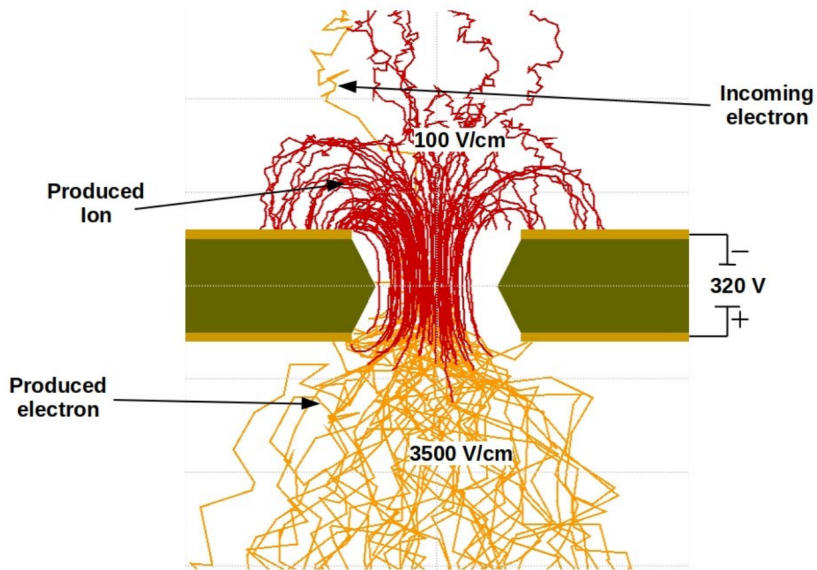


Figure 1.4: Garfield simulation of an avalanche in a GEM hole [30]. An incoming electron (orange) is accelerated in the strong electric field of the GEM and causes further ionization multiplying the number of free electrons (orange). Most of the produced cations (red) are captured by the GEM cathode.

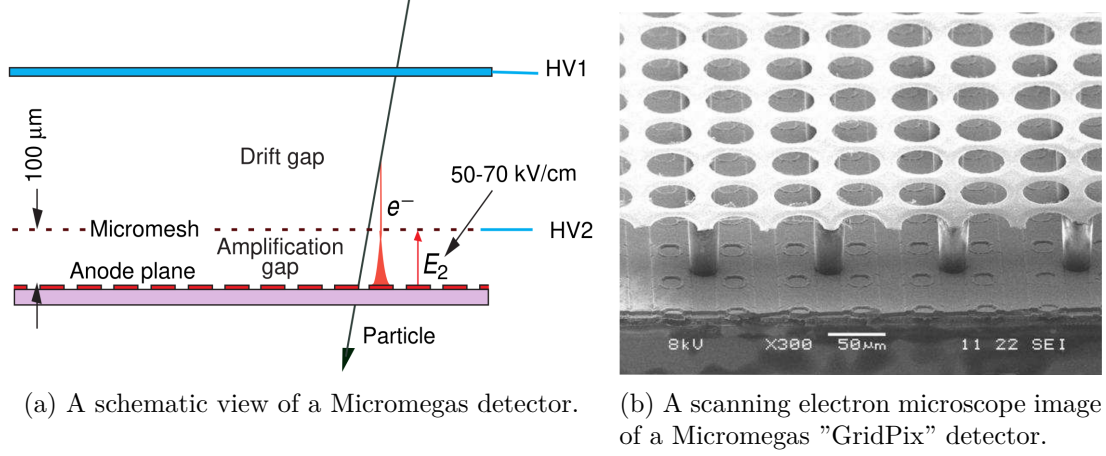


Figure 1.5: MICRO-MEsh GAseous Structure (Micromegas) [25].

361 as a signal on the segmented anode (Fig. 1.5a). Very high field ( $30\text{-}80 \text{ kV/cm}^2$ )  
 362 is necessary to achieve sufficient gain. Ion backflow is heavily suppressed by  
 363 the mesh.

364 A Timepix chip (a high granularity pixel detector) can be used for the readout  
 365 anode to achieve the best spatial resolution, making an integrated readout called  
 366 GridPix (Fig. 1.5b). Thanks to the high spatial resolution, it is possible to  
 367 distinguish individual electron clusters, which enables a new method of particle  
 368 identification.

### 369 Other MPGDs

370 A Resistive Plate WELL (RPWELL) consists of a THGEM with only the top  
 371 side metal-coated, mounted on a resistive film deposited on a thin isolating sheet  
 372 (which is read out similarly to a Resistive Plate Chamber (RPC)). Due to the  
 373 higher field in the closed holes of the THGEM, a higher gain can be reached for  
 374 the same voltage. A Micro-RWELL ( $\mu$ -RWELL) is a similar architecture with  
 375  $\sim 7$  times smaller pitch (distance between holes). These options provide a better  
 376 spark resistance and could allow to cover large areas for a lower cost.

377 A Micro-Pixel Gas Chamber ( $\mu$ -PIC) is a PCB with anode strips on one side  
 378 and orthogonal cathode strips on the other. The cathode has a resistive coating  
 379 and a regular pattern of uncoated regions with anode "dots" penetrating the PCB  
 380 at the centers.

## 381 1.4 Orthogonal Fields TPC at IEAP CTU

382 At IEAP CTU, we are going to use six identical atypical TPCs with inhomogeneous  
 383 toroidal magnetic field **orthogonal** to the electric field (details below),  
 384 hereafter referred to as Orthogonal Fields TPC (OFTPC). It has the shape of  
 385 isosceles trapezoidal prism 16 centimeters high with triple-GEM readout on one  
 386 of its bases. Dimensions of the OFTPC are discussed in detail in section 1.4.2  
 387 below. Throughout this thesis, we assume a uniform electric field along the  $z$  axis  
 388 with  $E_z = -400 \text{ V/cm}$ . Isn't the field affected by the MWPCs? Eventually a sim-  
 389 ulation will be needed. Measured particles enter the OFTPC through a window

390 after crossing the MWPC. Gas mixture used in the detector (70/30) and its effect  
391 – some graph with the mixture, reasons for the choice. Add a figure of the real  
392 TPC. More about the design choices.

### 393 1.4.1 Motivation and Associated Challenges

394 The reasons for the unusual field layout are mostly cost related:

- 395 a) we use permanent magnets instead of a solenoid and parallel fields are  
396 difficult to accomplish this way,
- 397 b) granularity of the TPC readout is limited in order to fit one SAMPA/SRS  
398 hybrid in each sector – parallel fields would bend the trajectories parallel  
399 to the readout requiring more pads and different architecture.

400 In this thesis, we will show that such a setup can reach a similar energy resolution  
401 as common cylindrical TPCs while reducing the overall cost.

402 The layout introduces two complications to the track reconstruction – the  
403 trajectory in inhomogeneous field is not circular and the drift is distorted by the  
404 magnetic field as shown in the Equation 1.1(in our case  $\omega\tau \approx 0.08$  for 0.3 T  
405 assuming  $\mu \approx 0.25 \text{ T}^{-1}$ , varies inside the detector). We will deal with these  
406 effects in the upcoming chapters.

407 The diffusion in such setup is larger since parallel orientation reduces diffusion  
408 by curling the electrons in the  $x$ - $y$  direction (see Equation 1.8), but for our  
409 relatively weak magnetic field and short drift distance, the difference is negligible.

### 410 1.4.2 Coordinate Systems and Dimensions

411 In order to describe events in our detector, we use three distinct spaces: the de-  
412 tector space  $\mathcal{D}$ , the readout space  $\mathcal{R}$  and the pad space  $\mathcal{P}$  (different spaces that  
413 describe different things and each has their own coordinate system, so maybe  
414 rename the section somehow?). Each space is later used to represent ionization  
415 electrons at different stages of the detection process: their creation in the gas,  
416 their final position when hitting the readout plane, and finally their representation  
417 in the discrete pad space.

#### 418 Detector Space

419 The detector space  $\mathcal{D}$  represents the physical space of our detector. We de-  
420 scribe it using Cartesian coordinates  $(x, y, z)$ . The  $z$ -axis is the detector's axis of  
421 symmetry, with its negative direction aligned with the proton beam. The origin  
422  $(0, 0, 0)$  is located at the center of the irradiated target. The positive  $x$ -axis passes  
423 through the center of one the OFTPCs along the intersection of its two planes  
424 of symmetry. The  $y$ -axis is then chosen to maintain a right-handed coordinate  
425 system.

426 Since the detector has a hexagonal symmetry, we use only one of its sectors  
427 in this work – the first sector  $\mathcal{D}_1 \subset \mathcal{D}$  which is defined by the condition:

$$(x, y, z) \in \mathcal{D}_1 \Leftrightarrow |y| \leq x \tan \frac{\pi}{6}. \quad (1.9)$$

428 Simulations in this sector can be applied to all sectors by rotating the coordinates  
429 accordingly. The volume of the OFTPC in this sector, which has the shape of

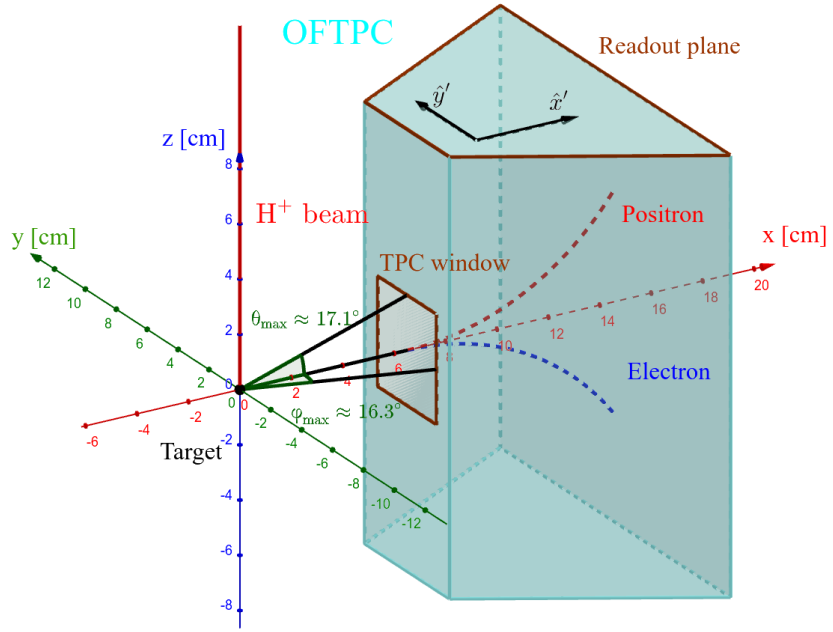


Figure 1.6: Schematics of the first sector OFTPC with detector space coordinates.

430 a trapezoidal prism, has these boundaries:

$$x \in [x_{\min}, x_{\max}] = [6.51, 14.61] \text{ cm}, \quad (1.10)$$

$$z \in [z_{\min}, z_{\max}] = [-8, 8] \text{ cm}, \quad (1.11)$$

$$y_{\max}(x_{\min}) = -y_{\min}(x_{\min}) = 2.75 \text{ cm}, \quad (1.12)$$

$$y_{\max}(x_{\max}) = -y_{\min}(x_{\max}) = 7.45 \text{ cm}, \quad (1.13)$$

431 where  $y_{\max}(x)$  is the maximal value of the  $y$ -coordinate for a given  $x$ . The read-  
432 out is located at  $z = 8$  cm; for some purposes, we also define the distance to  
433 the readout  $d_r = 8$  cm  $- z$  as an alternative to the  $z$ -coordinate. Keeping this  
434 paragraph as it is because the OFTPC volume is distinct from the first sector  
435 and some parts of this thesis use the space beyond this volume. The OFTPC  
436 window has width 3.8 cm and height 4.0 cm.

437 We also use spherical coordinates  $(r, \theta, \varphi)$  with the elevation angle  $\theta$  measured  
438 relative to the  $xy$  plane. Angles  $\theta$  and  $\varphi$  are useful when describing the direction  
439 of  $e^+/e^-$  tracks. Their maximal values considered for the initial direction in  
440 simulations are  $\theta_{\max} \approx 17.1^\circ$  and  $\varphi_{\max} \approx 16.3^\circ$  as shown in Fig. 1.6.

## 441 Readout Space

442 The readout space  $\mathcal{R}$  represents the drift time and final positions of ionization  
443 electrons as measured by an ideal continuous readout. We describe it using  
444 coordinates  $(x', y', t)$ , where  $x'$  and  $y'$  correspond to the detector coordinates at  
445 the readout plane ( $z = 8$  cm).

446 Currently not entirely sure how to put this into a figure since only  $x'$  and  
447  $y'$  correspond to the detector coordinates, it will make more sense when  
448 visualizing the map. The drift time  $t$  is approximately proportional to  $d_r$ .

449 **Pad Space**

450 The pad space  $\mathcal{P}$  represents the time bin and pad number of ionization electrons  
 451 as measured by an ideal discrete readout:

$$\mathcal{P} = \{(n_{\text{pad}}, n_t) \in \mathbb{N}^2 \mid n_{\text{pad}} \leq 128\}. \quad (1.14)$$

452 **Rewrite to reflect this:** Technically both values can be zero as defined in  
 453 the code (max channel 127). It is not really a subspace of  $\mathcal{R}$  but there is a  
 454 mapping from  $\mathcal{R}$  to  $\mathcal{P}$ . It is a discretization of a part of  $\mathcal{R}$ , the mapping can be  
 455 adjusted depending on the simulation. If we assume uniform electric field there  
 456 will be gaps, we don't use gaps in the reconstruction since the electrons should  
 457 be pulled towards the pads.

458 The readout of the OFTPC will consist (is the design final?) of 128 rectangular  
 459 pads arranged in a staggered pattern. Parameters of the pad layout are  
 460 shown in Fig. 1.7. The bottom left corner of  $n$ -th pad has coordinates  $(x_{1,n}, y_{1,n})$ ,  
 461 the top right  $(x_{2,n}, y_{2,n})$  and its center has coordinates  $(x_{c,n}, y_{c,n})$ . The gap be-  
 462 between neighboring pads is  $g = 0.08$  cm. Time will be read out in discrete bins of  
 463 size  $t_{\text{bin}} = 100$  ns (details?). Could also describe pad-related functions.

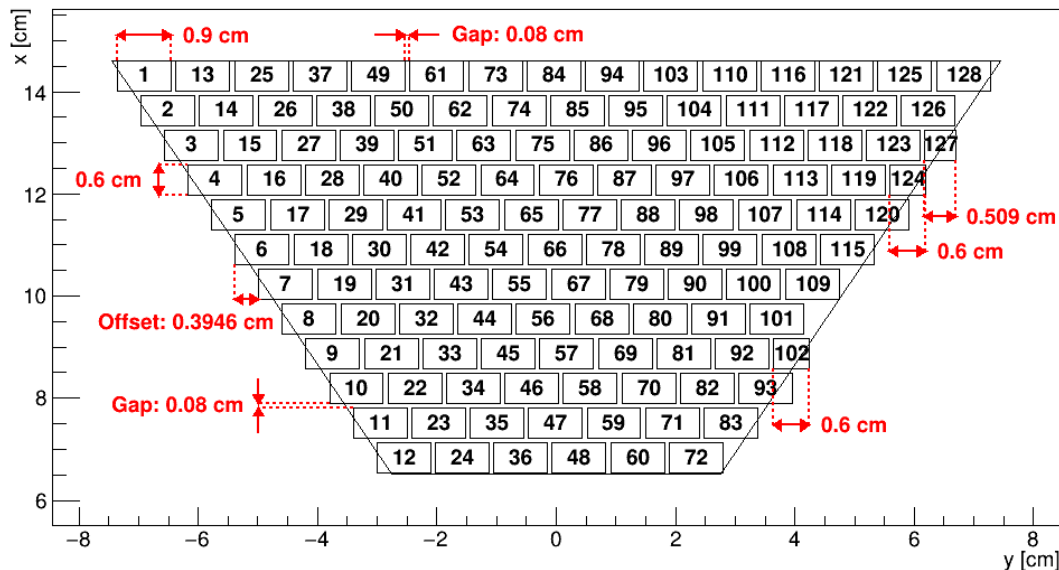
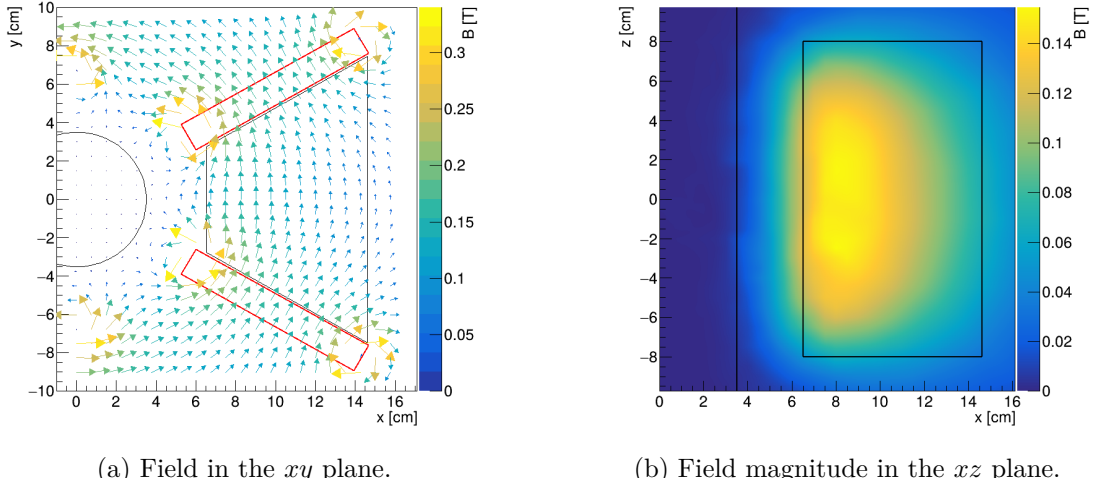


Figure 1.7: Pad layout of the OFTPC and its parameters. Pads 102, 124 and 127 are irregular, the rest has the same dimensions.

464 **1.4.3 Magnetic Field Simulation**

465 The magnetic field inside our detector is produced by six permanent magnets. It  
 466 was simulated using Ansys Maxwell (citation) which gives us values on a regular  
 467 grid. More details, vacuum tube, magnets (homogeneous?, density?). Visualiza-  
 468 tion of the magnetic field is shown in Fig. 1.8. Whenever we need to work with  
 469 values outside this grid, we use trilinear interpolation described below.



(a) Field in the  $xy$  plane.

(b) Field magnitude in the  $xz$  plane.

Figure 1.8: Magnetic field simulation results. The OFTPC volume and the vacuum tube are marked with black lines, the magnets are marked with red lines. **The coordinates of the magnets from the CAD drawing seem to be 9/10 of the ones from the magnetic simulation (confirm and fix).**

#### 470 Trilinear Interpolation

471 Trilinear interpolation is a 3D generalization of linear interpolation<sup>2</sup>. It can be  
 472 used to interpolate a function whose values are known on a regular grid with  
 473 rectangular prism cells. We use this simple method for interpolating the magnetic  
 474 field, and it is later used in Section 3.2.1 to interpolate the Ionization Electron  
 475 Map, a key component of our track reconstruction algorithm. In both cases, we  
 476 use a regular cubic grid (apparently it is also called a [Cartesian grid](#)).

477 Let us consider a cell of our regular grid (a cube) with an edge of length  $a$   
 478 containing the point  $\mathbf{C} = (x, y, z)$  where we want to interpolate a function  
 479  $f: \mathbb{R}^3 \rightarrow \mathbb{R}$ . We know the values of this function at the vertices of the cell  $\mathbf{C}_{ijk} =$   
 480  $= (x_0 + ia, y_0 + ja, z_0 + ka)$ , where  $\mathbf{C}_{000} = (x_0, y_0, z_0)$  is the origin of the cell ([is](#)  
 481 [that clear?](#)), and  $i, j, k \in \{0, 1\}$  are indices. We also define the points  $\mathbf{C}_{ij} =$   
 482  $= (x, y_0 + ia, z_0 + ja)$  and  $\mathbf{C}_i = (x, y, z_0 + ia)$ . Then the interpolated value  $\hat{f}(\mathbf{C})$   
 483 can be calculated as a composition of three linear interpolations (see Fig. 1.9):

$$\hat{f}(\mathbf{C}_{ij}) = (1 - x_d) f(\mathbf{C}_{0ij}) + x_d f(\mathbf{C}_{1ij}), \quad (1.15)$$

$$\hat{f}(\mathbf{C}_i) = (1 - y_d) \hat{f}(\mathbf{C}_{0i}) + y_d \hat{f}(\mathbf{C}_{1i}), \quad (1.16)$$

$$\hat{f}(\mathbf{C}) = (1 - z_d) \hat{f}(\mathbf{C}_0) + z_d \hat{f}(\mathbf{C}_1), \quad (1.17)$$

484 where  $x_d$ ,  $y_d$ , and  $z_d$  are given as follows:

$$x_d = \frac{x - x_0}{a}, \quad y_d = \frac{y - y_0}{a}, \quad z_d = \frac{z - z_0}{a}. \quad (1.18)$$

---

<sup>2</sup>Linear interpolation in point  $x \in (x_1, x_2)$  of a function  $f: \mathbb{R} \rightarrow \mathbb{R}$  known in points  $x_1 < x_2$  is the convex combination  $\hat{f}(x) = (1 - x_d)f(x_1) + x_d f(x_2)$ , where  $x_d = \frac{x - x_1}{x_2 - x_1} \in (0, 1)$ .

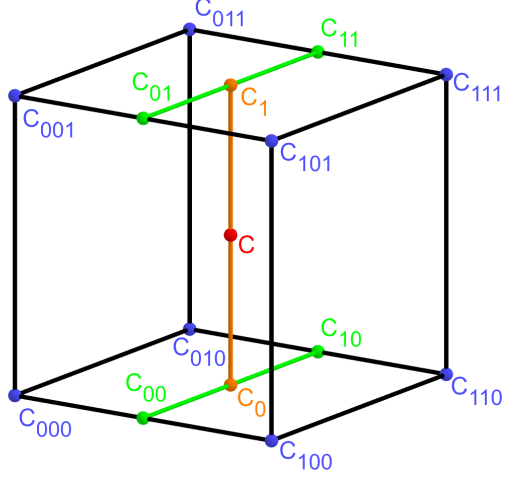


Figure 1.9: Visualization of trilinear interpolation as a composition of linear interpolations (inspired by [31]). We want to interpolate the value in the red point  $\mathbf{C}$ . First we interpolate between the four pairs of blue points sharing the last two indices along the  $x$ -axis (Eq. 1.15), then between the two pairs of the resulting green points along the  $y$ -axis (Eq. 1.16) and finally between the two resulting orange points along the  $z$ -axis to get the final red value (Eq. 1.17).

485 We can also write

$$\hat{f}(\mathbf{C}) = \sum_{i,j,k \in \{0,1\}} t_x^i t_y^j t_z^k f(\mathbf{C}_{ijk}), \quad (1.19)$$

$$t_\alpha \stackrel{\text{def}}{=} \begin{pmatrix} t_\alpha^0 \\ t_\alpha^1 \end{pmatrix} = \begin{pmatrix} 1 - \alpha_d \\ \alpha_d \end{pmatrix}, \quad (1.20)$$

486 where  $\alpha \in \{x, y, z\}$  is an index. This gives a nice geometric interpretation to the  
 487 trilinear interpolation as shown in Fig. 1.10. From this form and the figure, it is  
 488 apparent that the final interpolated value does not depend on the order of axes  
 489 along which we perform linear interpolations (see Fig. 1.9). Furthermore, we can  
 490 write  $\hat{f}(\mathbf{C})$  as a polynomial:

$$\hat{f}(\mathbf{C}) = \sum_{\alpha, \beta, \gamma \in \{0,1\}} \sum_{i=0}^{\alpha} \sum_{j=0}^{\beta} \sum_{k=0}^{\gamma} (-1)^{(\alpha-i)+(\beta-j)+(\gamma-k)} f(\mathbf{C}_{ijk}) x_d^\alpha y_d^\beta z_d^\gamma. \quad (1.21)$$

491 We take advantage of this form when generalizing trilinear interpolation to irreg-  
 492 ular grid in section 3.2.2.

493 Maybe a citation here, although I am not sure it is necessary since it could  
 494 be considered common knowledge. The last two equations are my own (but I'm  
 495 not sure that's worth mentioning unless there's a citation).

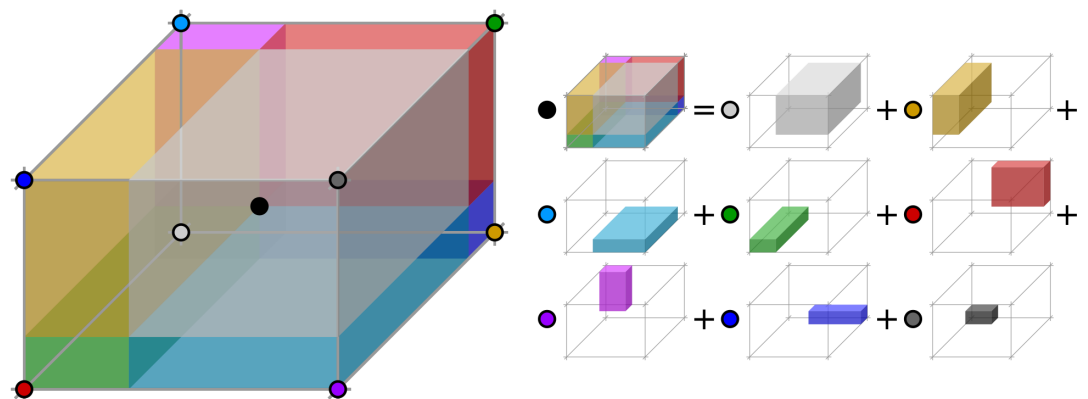


Figure 1.10: Geometric interpretation of trilinear interpolation as expressed in Equation 1.19. The colored dots represent the values in given points and the colored boxes represent the volume in the opposite corner by which the corresponding values are multiplied. The black dot represents the interpolated value which is multiplied by the entire volume [32].

## 2. Track Simulation

In order to develop and test the reconstruction algorithm, electron and positron tracks are simulated inside the first detector sector  $\mathcal{D}_1$  (see Section 1.4.2) with different initial parameters (origin, initial direction and kinetic energy). Two approaches are currently used to simulate tracks, each of them for different purpose.

The **Microscopic Simulation** uses the Garfield++ toolkit [1]. Within this toolkit:

- a) Magboltz, since it is mentioned later. Or maybe just class MediumMagboltz with the collision rates?
- b) the High Energy Electro-Dynamics (HEED) program [33] is used to simulate the primary particle,
- c) the class *AvalancheMicroscopic* to simulate the drift of secondary electrons created by ionization in the gas.

This is the most precise and time-consuming simulation used; our current goal is to be able to successfully reconstruct its results and determine our best-case energy resolution.

The **Runge-Kutta Simulation** uses the 4th order Runge-Kutta numerical integration (add citation for Runge-Kutta) to simulate the trajectory of the primary particle in the electromagnetic field inside the detector. It is relatively fast since it does not simulate the secondary particles. It is used as part of our reconstruction algorithm and for testing some parts of the reconstruction.

All of these simulations require the knowledge of the electromagnetic field (both **E** and **B**) inside the detector. A uniform electric field of  $400 \text{ V}\cdot\text{cm}^{-1}$  is assumed. The magnetic field was simulated in Maxwell (see Section 1.4.3). add citation

Single track in positive x direction or initial parameter randomization. Importance of gas composition, used gas compositions.

### 2.1 Microscopic Simulation

The microscopic simulation, the most detailed simulation used in this work, is performed using the Garfield++ toolkit [1].

The electron transport properties are simulated using the program Magboltz (add citation), (details?). Two different gas mixtures were compared – 90:10 and 70:30 Ar:CO<sub>2</sub>. The second mixture will be used in our detector (this was probably known a priori, but the first tests that I started with used 90/10, so maybe just note that the results justify the fact so far). The temperature is set to 20 °C, the pressure is atmospheric.

The primary track is simulated using the program HEED, which is an implementation of the photo-absorption ionization model [33] (see the reference, moved it to the end of sentence). This program provides the parameters of ionizing collisions. HEED can also be used to simulate the transport of delta electrons; we do not account for these in the current simulation (but plan to include them in the future – maybe mention only in the conclusion/future section). The photons created in the atomic relaxation cascade (fluorescence reabsorption, related to the spread of avalanches in GM det.?) are also not simulated.

540 Finally, we use the microscopic tracking provided by the class *AvalancheMicroscopic* in Garfield++ to simulate the drift of the ionization electrons. Each  
 541 electron is followed from collision to collision using the equation of motion and  
 542 the collision rates calculated by Magboltz (how fast is this? maybe it slows down  
 543 the simulation when spreading it across multiple jobs?).

544 Add more detailed and better description of HEED, and microscopic tracking  
 545 (each their own subsection?). Could also mention Monte Carlo (requires gas file  
 546 generation - Magboltz) and Runge-Kutta simulation implemented in Garfield,  
 547 why we don't use them (another subsection? rename the section to Garfield++  
 548 simulation and mention all relevant parts?).

### 550 2.1.1 First testing track

551 The first electron track simulated for testing purposes was chosen to have a special  
 552 set of parameters:

- 553 • the starting point of the track is the origin of the coordinate system,
- 554 • the initial direction is along the positive  $x$ -axis,
- 555 • the momentum is 8 MeV/c (the kinetic energy is 7.505 MeV).

556 Such a track moves in the XZ plane in the toroidal magnetic field of the detector,  
 557 because the particle's velocity vector is always perpendicular to the field. At first,  
 558 we simulated such a track in 90:10 Ar:CO<sub>2</sub> gas mixture, later we added a simu-  
 559 lation in 70:30 Ar:CO<sub>2</sub>, which we plan to use in our detector. The comparison of  
 560 both simulations is in Fig. 2.1.

### 561 2.1.2 Grid-like testing sample

562 In order to test all steps of the reconstruction, a sample of tracks with a grid-like  
 563 distribution of parameters was generated on MetaCentrum. Five sets of 9702  
 564 tracks were generated with every combination of these parameters:

- 565 • electron and positron tracks,
- 566 • 11 different kinetic energies  $E_{\text{kin}} \in [3, 13]$  MeV,
- 567 • 21 different azimuth angles  $\varphi \in [-16.3^\circ, 16.3^\circ]$  and
- 568 • 21 different elevation angles  $\theta \in [-17.1^\circ, 17.1^\circ]$ .

569 A visualization of a set of  $e^+/e^-$  tracks with the same kinetic energy is shown  
 570 in Fig. 2.2 (plotting actual HEED tracks using ROOT should be also possible  
 571 (but hard to make look good?)). In the 70:30 Ar:CO<sub>2</sub> atmosphere, each track  
 572 takes 5-30 CPU hours to simulate. Every tenth point on the drift line was stored,  
 573 the whole sample has 3.1 terabytes (or 1.4 gigabytes without drift lines).

## 574 2.2 Runge-Kutta Simulation

575 The Runge-Kutta simulation in this work uses the Runge-Kutta 4th order (RK4)  
 576 method to numerically integrate the equation of motion of a relativistic charged  
 577 particle in an electromagnetic field. Given a system of first order differential  
 578 equations

$$\frac{dy}{dt} = \mathbf{f}(t, \mathbf{y}(t)) \quad (2.1)$$

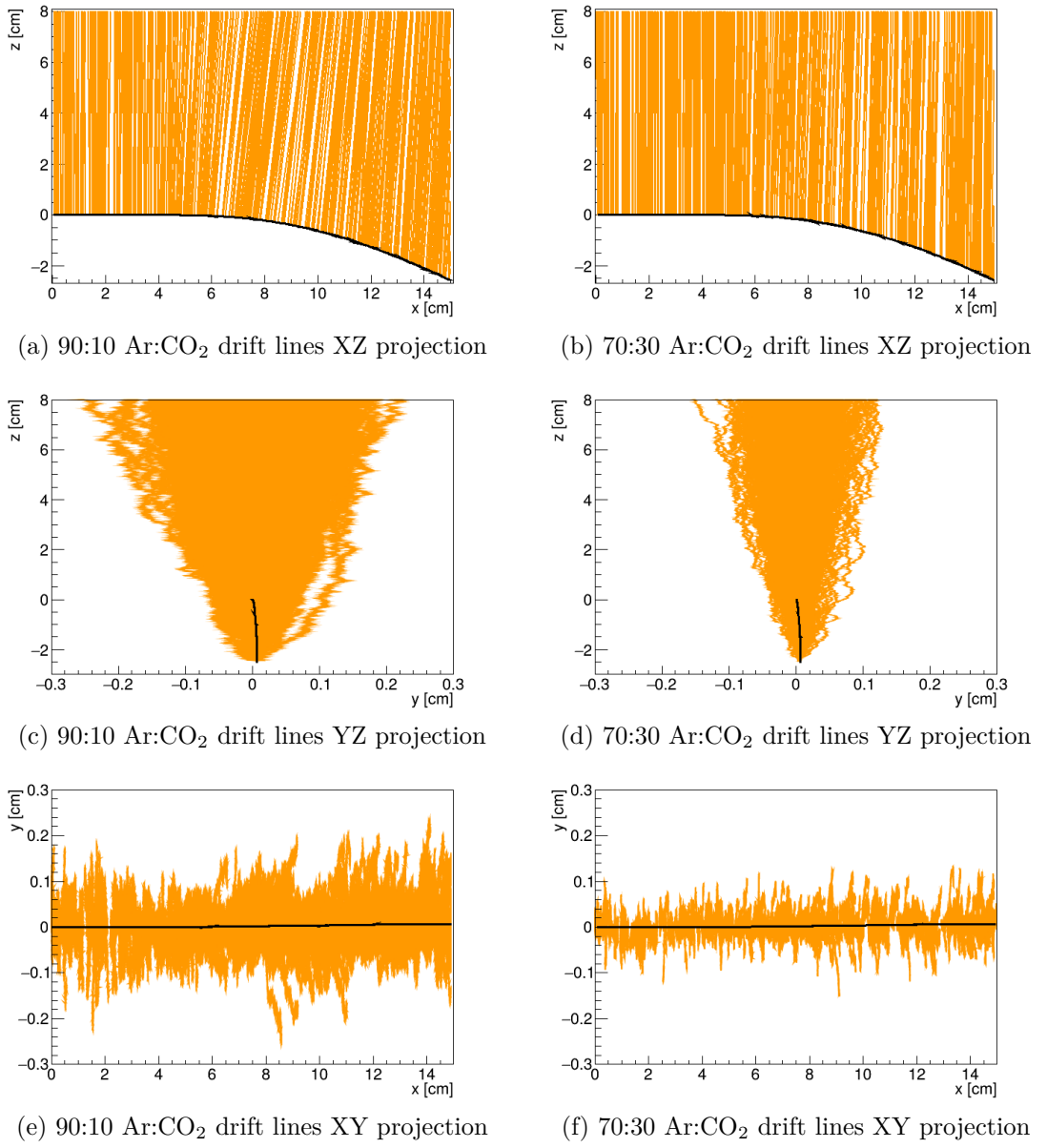


Figure 2.1: Comparison of drift lines for two different gas mixtures 90:10 and 70:30 Ar:CO<sub>2</sub>. The electron track is marked in black, the drift lines of the ionization electrons are marked in orange. In this example, we assume a larger OFTPC volume with readout at  $z = 8$  cm.

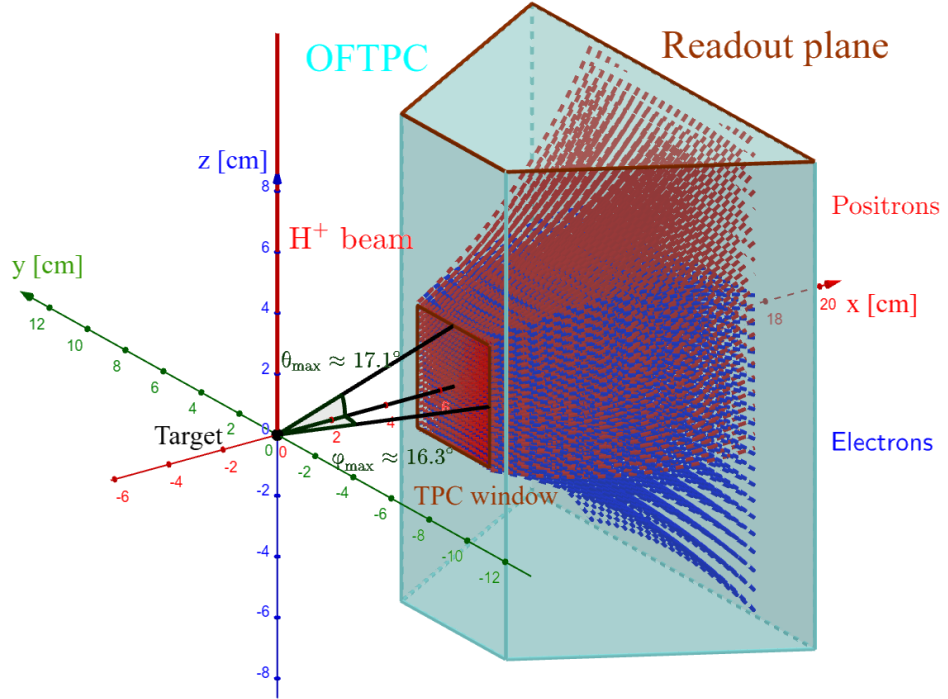


Figure 2.2: A visualization of a set of tracks from the grid-like testing sample with the same kinetic energy.

579 with an initial condition

$$\mathbf{y}(t_0) = \mathbf{y}_0, \quad (2.2)$$

580 we iteratively compute the estimate  $\mathbf{y}_n = \mathbf{y}(t_n) = \mathbf{y}(t_0 + nh)$  as follows (citation?  
581 common knowledge?):

$$\mathbf{k}_1 = \mathbf{f}(t_n, \mathbf{y}_n), \quad (2.3)$$

$$\mathbf{k}_2 = \mathbf{f}\left(t_n + \frac{h}{2}, \mathbf{y}_n + \frac{h\mathbf{k}_1}{2}\right), \quad (2.4)$$

$$\mathbf{k}_3 = \mathbf{f}\left(t_n + \frac{h}{2}, \mathbf{y}_n + \frac{h\mathbf{k}_2}{2}\right), \quad (2.5)$$

$$\mathbf{k}_4 = \mathbf{f}(t_n + h, \mathbf{y}_n + h\mathbf{k}_3), \quad (2.6)$$

582

$$\mathbf{y}_{n+1} = \mathbf{y}_n + \frac{1}{6}(\mathbf{k}_1 + 2\mathbf{k}_2 + 2\mathbf{k}_3 + \mathbf{k}_4). \quad (2.7)$$

583 Alternate forms (infinitely many) possible, accuracy vs computational cost. Runge-  
584 Kutta-Fehlberg with adaptive step size also possible, can potentially save some  
585 computation time especially in rapidly changing field (so maybe not in this case).

586 In our case, we want to integrate the equation of motion, given by the rela-  
587 tivistic Lorentz force:

$$F_L^\mu = m \frac{du^\mu}{d\tau} = q F^{\mu\nu} u_\nu, \quad (2.8)$$

588 where the Einstein summation convention is used,  $m$  is the mass of the particle,  
589  $q$  is its charge,  $u^\mu$  is its four-velocity,  $\tau$  is the proper time (i.e., time in the particle's  
590 frame of reference) and  $F^{\mu\nu}$  is the electromagnetic tensor at given coordinates  $x^\mu$

591 (we consider it to be time-independent in our detector). Given the electric  $\mathbf{E} =$   
 592  $= (E_x, E_y, E_z)$  and the magnetic field  $\mathbf{B} = (B_x, B_y, B_z)$  and using the metric  
 593 signature  $(+, -, -, -)$ , the equation expands to

$$\frac{d}{d\tau} \begin{pmatrix} \gamma c \\ \gamma v_x \\ \gamma v_y \\ \gamma v_z \end{pmatrix} = \frac{q}{m} \begin{pmatrix} 0 & -\frac{E_x}{c} & -\frac{E_y}{c} & -\frac{E_z}{c} \\ \frac{E_x}{c} & 0 & -B_z & B_y \\ \frac{E_y}{c} & B_z & 0 & -B_x \\ \frac{E_z}{c} & -B_y & B_x & 0 \end{pmatrix} \begin{pmatrix} \gamma c \\ \gamma v_x \\ \gamma v_y \\ \gamma v_z \end{pmatrix}, \quad (2.9)$$

594 where  $c$  is the speed of light in vacuum,  $\mathbf{v} = (v_x, v_y, v_z)$  is the particle's velocity  
 595 and  $\gamma = (1 - \frac{v^2}{c^2})^{-\frac{1}{2}}$  is the Lorentz factor (wrong magnetic field sign in the  
 596 implementation???). Together with the equation

$$\frac{d}{d\tau} \begin{pmatrix} ct \\ x \\ y \\ z \end{pmatrix} = \begin{pmatrix} \gamma c \\ \gamma v_x \\ \gamma v_y \\ \gamma v_z \end{pmatrix} = u^\mu, \quad (2.10)$$

597 we get a system of eight first order differential equations for  $x^\mu$  and  $u^\mu$ , which  
 598 we can integrate using the Runge-Kutta method described above. As a result of  
 599 this integration, we get the position  $\mathbf{x}(\tau_n)$ , the velocity  $\mathbf{v}(\tau_n)$  and the detector  
 600 time  $t(\tau_n)$  for every proper time  $\tau_n = n\tau_{\text{step}}$ . Integrating using the proper time  
 601 means that the step size in  $t$  gets larger by the gamma factor  $\frac{dt}{d\tau} = \gamma$  (maybe  
 602 change it and integrate the detector time or adjust the step size accordingly). The  
 603 only difference is in the step size (because  $t$  gets also calculated as it is among the  
 604 8 variables). It might be even better to adjust the step size using approximate  
 605 distance traveled. As initial conditions, we use the origin of the track  
 606  $(x_0, y_0, z_0)$ , the initial velocity direction vector  $\mathbf{n} = (\cos \varphi \cos \theta, \sin \varphi \cos \theta, \sin \theta)$   
 607 and the kinetic energy  $E_{\text{kin}}$  (initial parameters of the simulation (fit is in chapter  
 608 4)), we then compute  $\gamma$  and  $\|\mathbf{v}\|$ :

$$\gamma = 1 + \frac{E_{\text{kin}}}{E_0}, \quad (2.11)$$

$$\|\mathbf{v}\| = c\sqrt{1 - \gamma^{-2}}. \quad (2.12)$$

### 609 2.2.1 Testing sample

610 Example of RK simulation – first testing track, randomized sample of 100000  
 611 tracks (could also move them to circle 3D fit).

612 In order to test the simulation and reconstruction, a sample of 100 000 tracks  
 613 with randomized parameters was generated:

- 614 • the Runge-Kutta step was set to 0.1 ns (proper time, which wouldn't be a  
 615 problem but this way the "spatial" step depends on energy),
- 616 • the kinetic energy of the particle  $E_{\text{kin}} \in [4, 12]$  MeV,
- 617 • the starting point of the track is a random point in the OFTPC window,

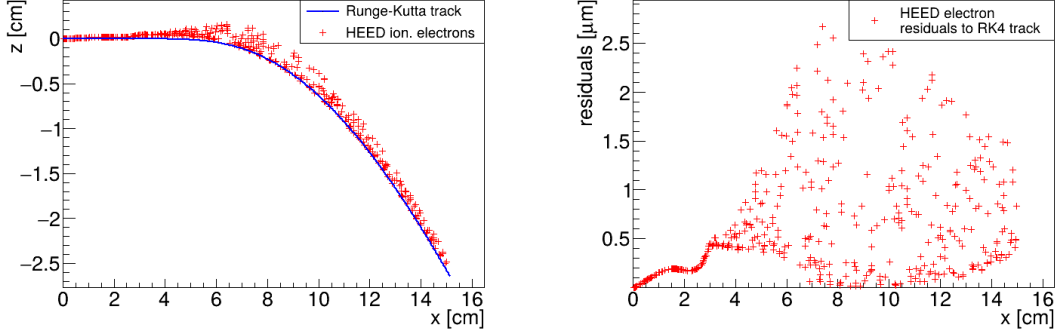


Figure 2.3: A comparison of the HEED track from the microscopic simulation in Section 2.1.1 with a Runge-Kutta track with the same initial parameters and  $\tau_{\text{step}} = 0.1$  ps (reducing the step further doesn't make a visible difference). In the view of the tracks on the left, the distance of the HEED ionization electrons from the RK4 track is exaggerated 1000 $\times$ . On the right, the dependence of the HEED electrons residuals (i.e., their shortest distance to the RK4 track) on their  $z$ -coordinate is shown. **The images look the same even for 100,000x smaller step, so the residuals are a result of something that HEED does (maybe a different interpolation technique for the magnetic field? the pattern looks similar for two different tracks so it can't be scattering).**

When exaggerating, the HEED ionization electrons are moved away along the shortest line connecting them to the RK4 track. The computation of this distance is described in Section 4.3.

- 618     • the initial direction is given by the line connecting a random point on  
619       the target<sup>1</sup> (a disc with 1 mm radius in the YZ plane).
- 620     Since the Runge-Kutta simulation is quite fast<sup>2</sup>, it can be run locally on any  
621       computer. **Add a figure with simulated tracks (sample).** An example Runge-  
622       Kutta track is compared with the corresponding microscopic track in Fig. 2.3.

---

<sup>1</sup>To generate a random point on the target, we generate a random angle  $\alpha$  and a random square of the distance from origin  $r^2$  to get a uniform distribution.

<sup>2</sup>One track with  $\tau_{\text{step}} = 0.1$  ps takes less than one millisecond to simulate.

## 623 3. Track Reconstruction

624 As the first step of the reconstruction algorithm, we reconstruct the track of  
625 a primary particle – either an electron or a positron. Then, using this information,  
626 we determine the energy of the particle (Section 4).

627 The **Reconstruction Assuming Steady Drift** uses the standard TPC ap-  
628 proach. With parallel fields, the drift inside a uniform electric field remains  
629 undistorted (as shown in Equation 1.1). Therefore, we only need to reconstruct  
630 the  $z$ -coordinate from the drift time using the known drift velocity. We also  
631 assume that the readout coordinates ( $x'$ ,  $y'$ ,  $t$ ) are known exactly, neglecting  
632 the pads and time binning.

633 Reconstruction using an **Ionization Electron Map** (from now on referred  
634 to as *the map*) uses a simulation of the drift of secondary (ionization) electrons  
635 within the detector volume. This simulation can then be used to interpolate  
636 the initial position of the secondary electrons. In the first iteration of this method  
637 the readout is assumed to be continuous.

638 We present two algorithms using the map for reconstruction. The first one uses  
639 a gradient descent algorithm along with trilinear interpolation (see Section 1.4.3)  
640 of the map. The second method uses interpolation on the irregular inverse grid  
641 with a polynomial.

642 The **Discrete Reconstruction** uses the map; instead of reconstructing the ex-  
643 act position of each electron, we reconstruct the center of each hit pad together  
644 with the time corresponding to the midpoint of the time bin. The electron count  
645 in each TPC bin (consisting of the pad and the time bin) serves as an idealized  
646 collected charge, which is then used as a weight in the energy reconstruction fit.

### 647 3.1 Reconstruction Assuming Steady Drift

648 As the first step, we tried to reconstruct a simulated electron track with a special  
649 set of initial parameters, described in detail in Section 2.1.1. The starting point  
650 is given by the origin of our coordinate system and its initial direction is given by  
651 the positive  $x$ -axis. This means the magnetic field of our detector is perpendicular  
652 to the momentum of the particle at all times, and we can reduce the problem to  
653 two-dimensional space.

654 For the reconstruction, we decided to use the common method used in a stan-  
655 dard TPC (similar to?, cite some source(s)!). This will allow us to explore  
656 the significance of the atypical behavior in our OFTPC. Additionally, we assume  
657 the readout is continuous to further simplify the problem. In this approximation,  
658 we reconstruct the initial position of each ionization electron.

659 The reconstruction is then defined by the following relations between the co-  
660 ordinates of the detector space and the readout space (see Section 1.4.2):

$$x = x', \quad (3.1)$$

$$y = y', \quad (3.2)$$

$$z = 8 \text{ cm} - d_r = 8 \text{ cm} - v_d t, \quad (3.3)$$

661 where  $d_r$  is the distance to the readout, and  $v_d$  is the drift velocity of electrons  
662 in the given gas mixture. At a phenomenological level, this velocity can be con-

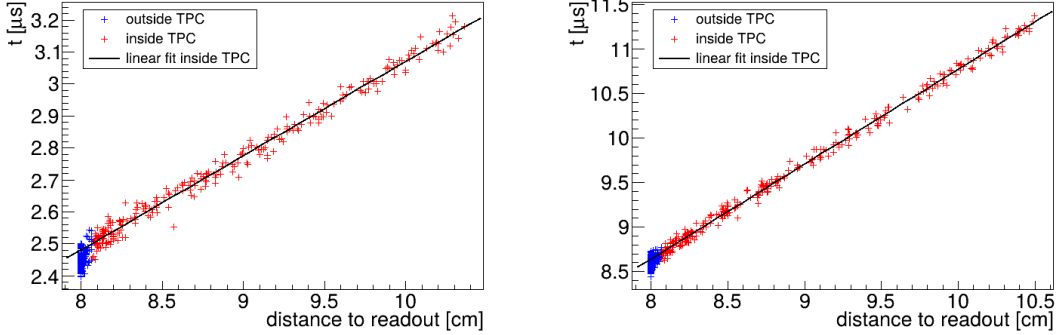


Figure 3.1: Linear fit of the drift time  $t$  dependence on the distance to the readout  $d_r = 8 \text{ cm} - z$  for the ionization electrons in 90:10 (left) and 70:30 (right) Ar:CO<sub>2</sub> gas composition. Only electrons inside the TPC (red) are fitted. The parameters are  $v_d = 3.39 \text{ cm}/\mu\text{s}$ ,  $d_0 = -0.41 \text{ cm}$  for 90:10, and  $v_d = 0.939 \text{ cm}/\mu\text{s}$ ,  $d_0 = -0.11 \text{ cm}$  for 70:30 Ar:CO<sub>2</sub>.

sidered as a function of the electric field  $\mathbf{E}$  and the magnetic field  $\mathbf{B}$  as shown in Equation 1.1. The Garfield++ toolkit uses this fact to accelerate their drift simulation with non-microscopic approaches (could mention in the simulation chapter). Since we assume a uniform electric field in the detector and in this approximation we want to neglect the effect of our unusual magnetic field, we consider the drift velocity constant. We can estimate the drift velocity by fitting the dependence  $d_r(t)$  of ionization electrons from a simulated track with a linear function:

$$d_r(t) = v_d t + d_0. \quad (3.4)$$

The fit was applied on two tracks with different gas composition, the result is in Fig. 3.1. Compare with real drift velocities – a good indication of the tilt of drift lines. The obtained parameters are then used for the reconstruction shown in Fig. 3.2. From the residuals shown in Fig. 3.3, we can see that this reconstruction algorithm leads to significant deviations from the simulated track (up to 1.1 cm for 90:10, and up to 0.3 cm for 70:30 Ar:CO<sub>2</sub>), especially in the faster gas mixture 90:10 (as expected – for a higher mean time between collisions in Equation 1.1, the effect of the magnetic field is bigger). These deviations are mainly caused by the shift in the  $x$ -coordinate due to the tilt of the drift lines in magnetic field. In order to account for this, we need to develop a better algorithm. There is also a small irregularity in the  $z$ -coordinate but it is comparable with the diffusion. We can/will also later show that this has a significant effect on the reconstructed energy.

## 3.2 Ionization Electron Map

Inside an OFTPC (more than one, also considering it a general concept rather than the specific OFTPC used at this experiment), the drift of the ionization electrons is significantly affected by its magnetic field as shown in Equation 1.1, see also Fig. 2.1. We need to take this into account for accurate reconstruction (should be easy to run the reconstruction without the map and show how much it improves the results). In the first approximation, we assume a continuous readout (i.e., we neglect the anode segmentation into pads). We can then

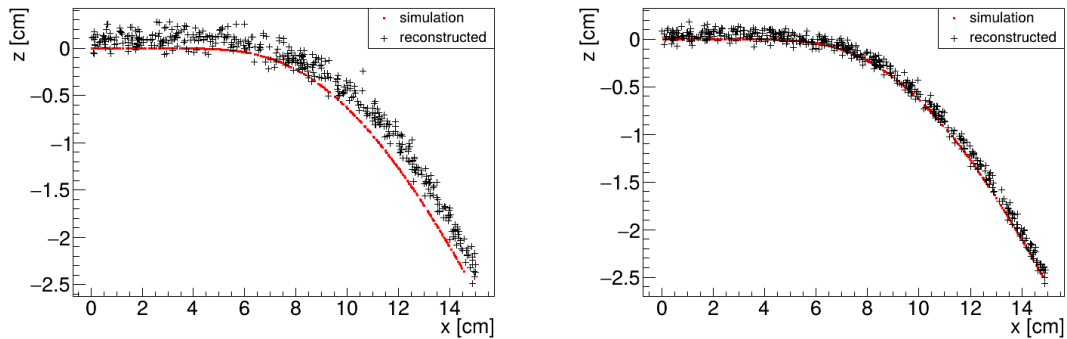


Figure 3.2: Reconstruction (black) of the starting position of ionization electrons (red) using parameters obtained from the fit (Fig. 3.1). Two gas compositions 90:10 (left) and 70:30 Ar:CO<sub>2</sub> (right) are compared.

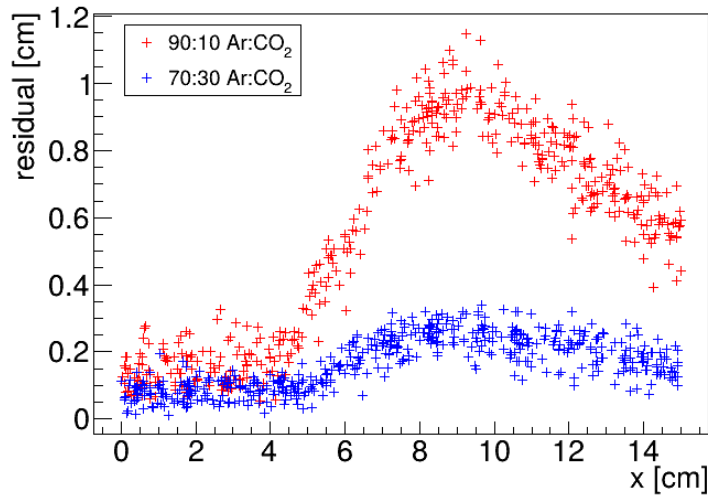


Figure 3.3: Comparison of residuals (i.e., the distance from the reconstructed point to the simulated ionization electron starting point) dependence on  $x$  for two gas mixtures 90:10 (red) and 70:30 Ar:CO<sub>2</sub> (blue).

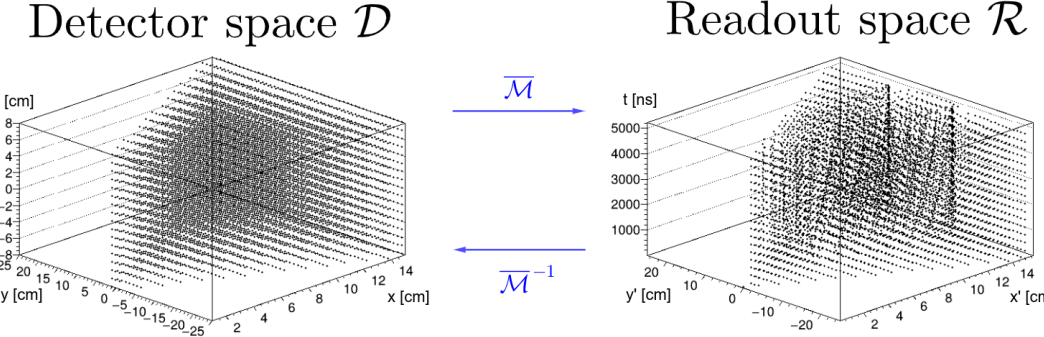


Figure 3.4: A 3D visualization of the mapping of means  $\bar{\mathcal{M}}$  for the 90:10 Ar:CO<sub>2</sub> gas. A regular grid  $\mathbb{G}$  with  $l = 1$  cm in the detector space is mapped to an irregular grid  $\mathbb{G}^{-1} \equiv \bar{\mathcal{M}}(\mathbb{G})$  in the readout space.

691 reconstruct the original position of each ionization electron using its readout co-  
692 ordinates. For this purpose, we use the ionization electron map.

693 The ionization electron map represents a mapping from the detector space  
694 to the readout space (see Section 1.4.2). It tells us what readout coordinates  
695 ( $x', y', t$ ) we can expect on average for an ionization electron created at the detec-  
696 tor coordinates ( $x, y, z$ ). More precisely, it is a mapping to the distributions on  
697 the readout space; we can simplify this as only the means  $\bar{\mathcal{M}}$  and the covariance  
698 matrices  $\mathcal{M}_\Sigma$ , assuming Gaussian distribution:

$$\bar{\mathcal{M}}: \mathcal{D} \longrightarrow \mathcal{R}, \quad (x, y, z) \longmapsto \bar{\mathbf{X}}^T \equiv (\bar{x}', \bar{y}', \bar{t}), \quad (3.5)$$

$$\mathcal{M}_\Sigma: \mathcal{D} \longrightarrow \mathbb{R}^{3 \times 3}, \quad (x, y, z) \longmapsto \Sigma \equiv \begin{pmatrix} \sigma_{x'}^2 & \text{cov}(x', y') & \text{cov}(x', t) \\ \text{cov}(y', x') & \sigma_{y'}^2 & \text{cov}(y', t) \\ \text{cov}(t, x') & \text{cov}(t, y') & \sigma_t^2 \end{pmatrix}, \quad (3.6)$$

$$\mathcal{M}: \mathcal{D} \longrightarrow D(\mathcal{R}), \quad (x, y, z) \longmapsto N(\mathbf{X}) \equiv \frac{\exp\left(-\frac{1}{2}(\mathbf{X} - \bar{\mathbf{X}})^T \Sigma (\mathbf{X} - \bar{\mathbf{X}})\right)}{\sqrt{(2\pi)^3 |\Sigma|}}. \quad (3.7)$$

699 To get an approximation of this mapping, we simulate the drift of ionization  
700 electrons generated on a regular Cartesian grid  $\mathbb{G} \subset \mathcal{D}$  with spacing  $l$  inside  
701 the volume of our OFTPC<sup>1</sup> (see the visualization in Fig. 3.4). In Fig. 3.5, you  
702 can see an example of drift lines from a test of the simulation. After testing runs,  
703 two map simulations were made with different gas composition, their parameters  
704 are shown in Table 3.1.

705 In order to get accurate results, we use the microscopic simulation of these  
706 electrons described in Section 2.1 (Monte Carlo from *AvalancheMC* was also con-  
707 sidered but it doesn't (didn't? CERES used it from MAGBOLTZ???) include  
708 magnetic field, we can probably improve this anyway using the fast track sim-  
709 ulation with map proposed in the future section). It is also useful to simulate  
710 multiple ( $N$ ) electrons originating from the same position so that we can account  
711 for the random fluctuations due to collisions. Using the readout coordinates of  
712 the electrons, we then estimate the means and the covariance matrix:

$$\bar{\mathbf{X}} = \frac{1}{N} \sum_{i=1}^N \mathbf{X}_i, \quad \Sigma = \frac{1}{N-1} \sum_{i=1}^N (\mathbf{X}_i - \bar{\mathbf{X}})(\mathbf{X}_i - \bar{\mathbf{X}})^T, \quad (3.8)$$

<sup>1</sup>The detector walls are not considered and we simulate the drift even outside of the OFTPC which allows us to interpolate even close to the walls

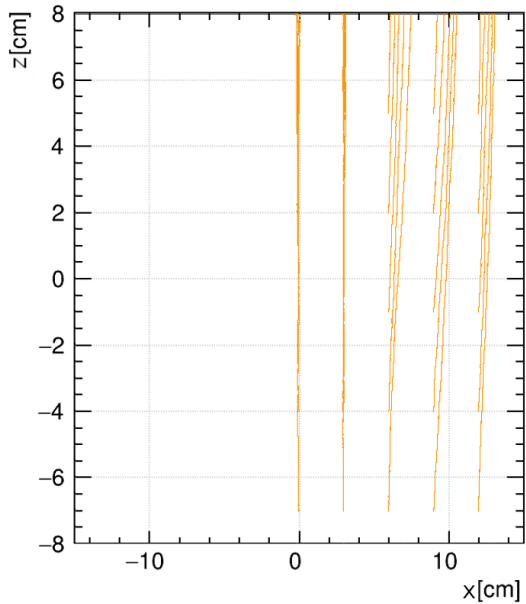


Figure 3.5: A test of the 90:10 Ar:CO<sub>2</sub> map simulation with spacing  $l = 1.5$  cm. The resulting drift lines of evenly spaced electrons are displayed in orange.

Table 3.1: Comparison of parameters of two map simulations.

Parameter	90:10 Ar:CO <sub>2</sub> map	70:30 Ar:CO <sub>2</sub> map
$N$	100	100
$l$	1.0 cm	0.5 cm
$z$ bounds	$[-8, 8]$ cm	$[-8, 8]$ cm
$x$ bounds	$[0, 15]$ cm	$[-1.5, 15.0]$ cm
$y$ bounds	$ y  \leq x \cdot \tan \frac{\pi}{3}$	$ y  \leq (x + 1.5 \text{ cm}) \cdot \tan \frac{\pi}{6}$

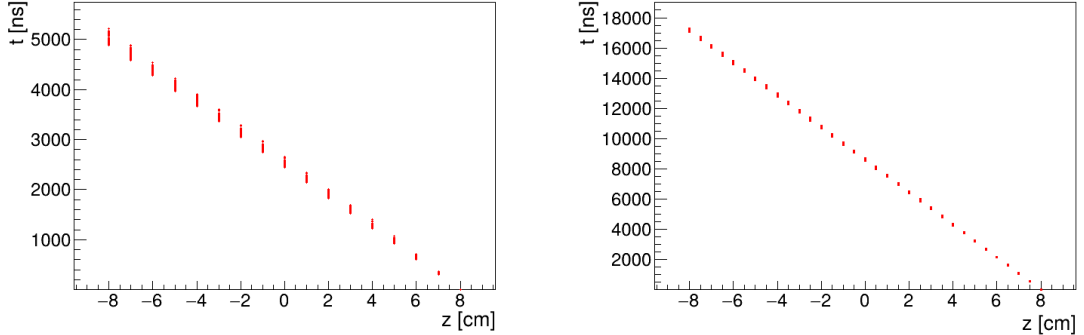


Figure 3.6: Dependence of the drift times of the simulated map  $\bar{\mathcal{M}}$  on the  $z$ -coordinate. Two gas mixtures 90:10 (left) and 70:30 Ar:CO<sub>2</sub> (right) are compared. The spread is caused by varying Lorentz angles.

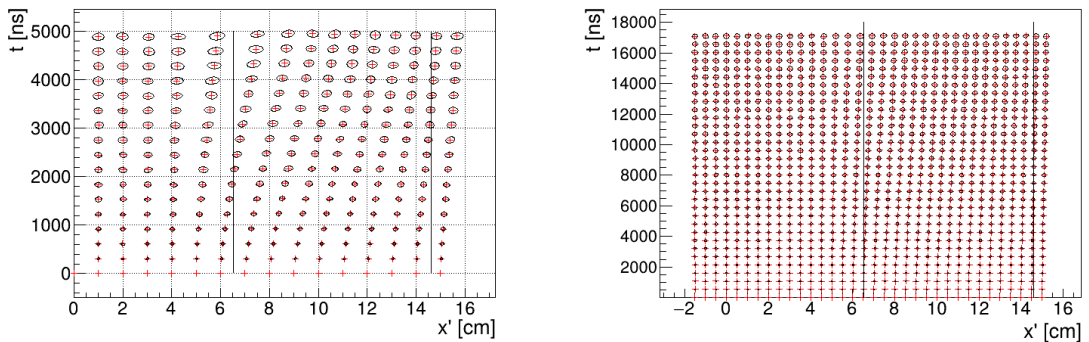


Figure 3.7: The  $x't$  projection of the  $\mathcal{M}(\mathbb{G}_{y=0})$  mapping of a part of the regular grid  $\mathbb{G}$ . The means  $\bar{\mathcal{M}}(\mathbb{G}_{y=0})$  are marked with red crosses, and the diffusion error is denoted by black 95% confidence error ellipses computed from the diagonalized covariance matrices  $\mathcal{M}_\Sigma(\mathbb{G}_{y=0})$ . Two gas mixtures 90:10 (left) and 70:30 Ar:CO<sub>2</sub> (right) are compared. The first mixture shows differences of  $t$  for electrons with same initial  $z$  but different initial  $x$ . For the second mixture, these differences are negligible in comparison with the diffusion.

713 where  $\mathbf{X}_i$  represents the readout coordinates  $(x'_i, y'_i, t_i)^T$  of the  $i$ -th electron. The  
 714 matrix (resp. its submatrix) can then be used to plot error ellipsoid (resp. el-  
 715 lipse). The axes correspond to the eigenvectors, errors along these axes for a given  
 716 confidence level  $p$  can be computed using the chi-squared distribution

$$\sigma_i = \sqrt{\lambda_i \chi_k^2(p)}, \quad (3.9)$$

717 where  $\lambda_i$  is the corresponding eigenvalue and  $k$  is the number of degrees of free-  
 718 dom.

719 As shown in Figs. 3.6 and 3.7, the drift times in the map are no longer propor-  
 720 tional to the  $z$ -coordinate due to the varying Lorentz angles in the inhomogeneous  
 721 magnetic field (see Equation 1.2). As expected, the effect is considerably larger in  
 722 gases with higher drift velocities. Similarly, the drift distortion (i.e., its deviation  
 723 from the vertical lines) is huge for the "faster" gas, but still significant for the  
 724 "slower" one, as demonstrated in Figs. 3.8 to 3.10.

725 When evaluating the map inside the grid, we use trilinear interpolation (see  
 726 Section 1.4.3). From now on, we will use the same symbol  $\mathcal{M}$  for this interpolated

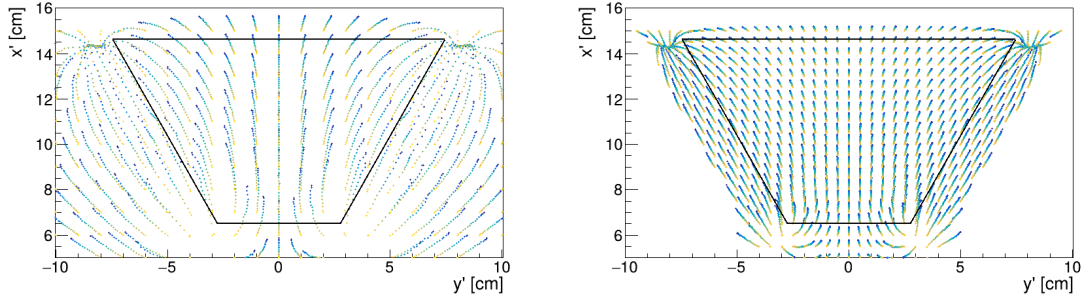
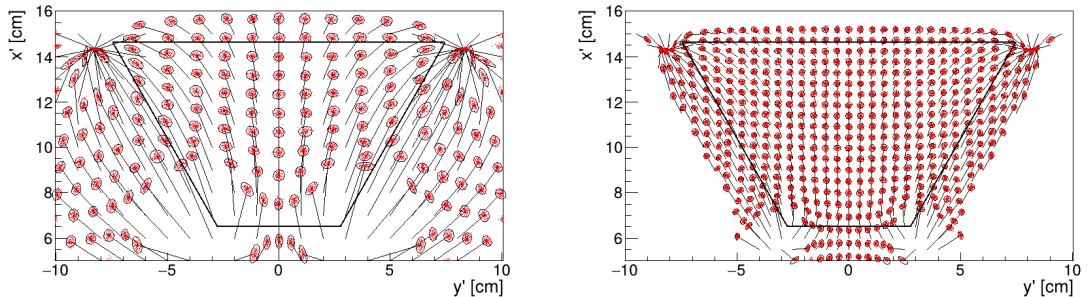
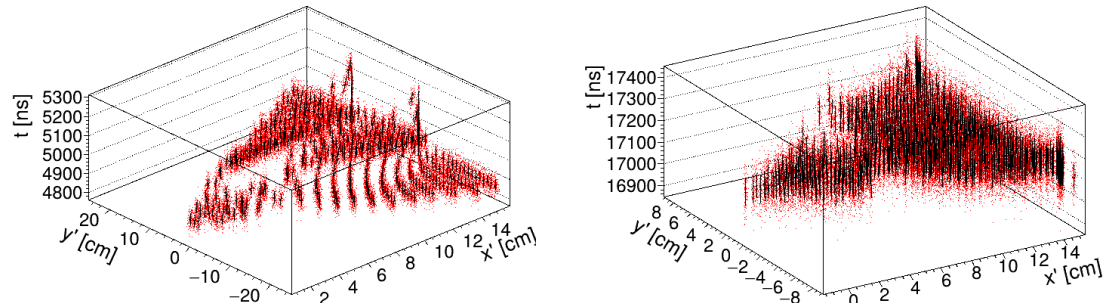


Figure 3.8: The regular grid  $\mathbb{G}$  projected by the mapping  $\bar{\mathcal{M}}$  from the detector space onto the  $x'y'$  plane ( $t$  is not plotted). Layers with lower  $z$ -coordinate (i.e., further away from the readout) are displayed with darker colors. The OFTPC volume is marked with black lines. Two gas mixtures 90:10 (left) and 70:30 Ar:CO<sub>2</sub> (right) are compared.



(a) The  $x'y'$  projection of  $\mathcal{M}(\mathbb{G}_8)$  (similar as in Fig. 3.8), the diffusion is denoted with the 95% error ellipses from the diagonalized sample covariance matrices  $\mathcal{M}_{\Sigma}(\mathbb{G}_8) \leftrightarrow$  Equation 3.8, and computed using Equation 3.9. The mean values  $\bar{\mathcal{M}}(\mathbb{G}_8)$  are connected by black arrows with the corresponding starting position  $(x, y)$  of the simulated electrons. The OFTPC volume is marked with black lines.



(b) The full mapping  $\mathcal{M}(\mathbb{G}_8)$ , the diffusion is marked using standard error bars (black) from the diagonalized sample covariance matrices (Equations 3.8 and 3.9).

Figure 3.9: The  $\mathcal{M}(\mathbb{G}_8)$  mapping of the bottom ( $z = -8$  cm) layer  $\mathbb{G}_8$  of the regular grid  $\mathbb{G} \subset \mathcal{D}$ . It includes both the mapping of means  $\bar{\mathcal{M}}$  and of covariances  $\mathcal{M}_{\Sigma}$ . Individual electrons from the map simulation are marked with red dots. Two gas mixtures 90:10 (left) and 70:30 Ar:CO<sub>2</sub> (right) are compared.

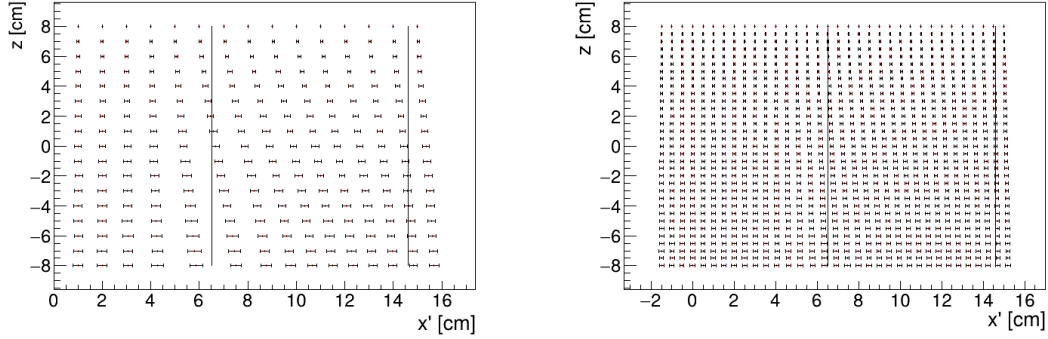


Figure 3.10: The readout coordinate  $x'$  for points on the grid  $\mathbb{G}_{y=0}$  plotted against their initial coordinate  $z$ . The means are marked with red crosses, the diffusion in  $x'$  is denoted by standard error bars. Two gas mixtures 90:10 (left) and 70:30 Ar:CO<sub>2</sub> (right) are compared.

727 simulation.

728 Finally, we need to invert the map to get the original detector coordinates  
 729  $(x, y, z)$  from the given readout coordinates  $(x', y', t)$ . In our case, it is reasonable  
 730 to assume that the mapping  $\mathcal{M}$  (we lose the information about the distribution  
 731 (a wild idea how to recover this is in the Future section but it will only make sense  
 732 if the GEM is already accounted for and is very preliminary as there are many  
 733 factors to consider)) is one-to-one (as seen in the simulations). We implemented  
 734 two methods for this purpose: the gradient descent search (Section 3.2.1) and  
 735 interpolation on the inverse grid (Section 3.2.2).

736 The simulation (?) of the map is a computationally heavy task. For this rea-  
 737 son, we use the MetaCentrum grid [3] to parallelize needed calculations. At first,  
 738 this was done by evenly distributing the simulated electrons across the individual  
 739 jobs in a simulation with only one electron per vertex in the regular grid  $\mathbb{G}$  with  
 740 a spacing of one centimeter. Later, a more efficient approach was implemented,  
 741 accounting for the varying lengths of the drift of individual electrons. If we index  
 742 the vertices of  $\mathbb{G}$  in the order of increasing coordinates  $y, x, z$  (picture will make  
 743 things clearer), we can express the number  $n_l$  of full XY layers (i.e., electrons  
 744 with the same  $z$  coordinate, the mapping of one such layer is shown in Fig. 3.9b)  
 745 with index less than or equal to  $i$

$$n_l(i) = \left\lfloor \frac{i}{n_{xy}} \right\rfloor, \quad (3.10)$$

746 where  $n_{xy}$  is the number of electrons in each XY layer calculated simply by count-  
 747 ing the electrons that satisfy boundary conditions for  $x$  and  $y$ . These conditions  
 748 should be mentioned above; sector condition + maximal  $x$  value. The number of  
 749 electrons remaining in the top layer is then

$$n_r(i) = i \bmod n_{xy}. \quad (3.11)$$

750 Finally, we can calculate the sum of the drift gaps of electrons up to index  $i$

$$d_{\text{sum}} = (z_{\max} - z_{\min})n_{xy}n_l - \frac{n_l(n_l - 1)}{2}n_{xy}l + n_r(z_{\max} - z_{\min} - n_l l). \quad (3.12)$$

751 We then use a binary search algorithm to find the maximum index  $i$  such that  
 752 the value of this sum is less than the fraction  $\frac{\text{job id}}{\max \text{ job id}}$  of the total sum. This way  
 753 we obtain the minimal and the maximal index of electrons simulated in the given  
 754 job. **Picture of the simulating grid (1 layer).** zmin zmax also

755 The obtained map is then stored in a custom class template *Field*, could  
 756 expand on that. Maybe earlier, since the same template is used for the magnetic  
 757 field.

758 Simulation inside of one sector (at first double angle). Extra space on the sen-  
 759 sor. Using qsub (not sure if important). Add plots of distortion of the coordinates.  
 760

761 Images to add (comparison of both simulations):

- 762 Already have a simple 2D map visualization from the RD51 presentation,  
 763 can use it or make something better
- 764 •  $z$  vs.  $t$  plot
- 765 • XY plane distortion for different  $z$  values; with arrows and error bars, for  
 766 all  $z$ -layers with different colors
- 767 • XZ plane ( $y = 0$ ) distortion in  $x$  (maybe not necessary?)
- 768 • XT plot ( $y = 0$ ) showing (small) distortion in drift times  
 769

770 More images:

- 771 • Residuals of the continuous readout reconstruction.

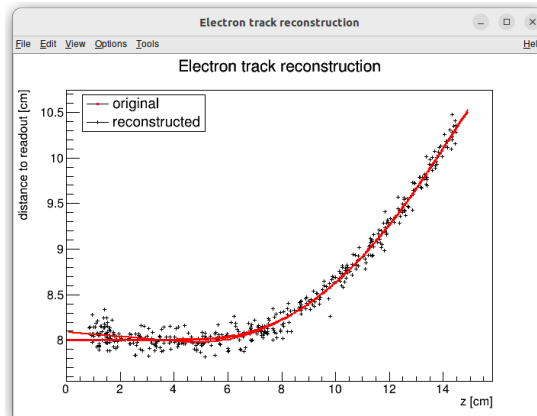


Figure 3.11: Example reconstruction with the map. Swap for better image, correct coordinates.

### 772 3.2.1 Gradient Descent Algorithm

773 The first implemented method of reconstruction uses a gradient descent algorithm  
 774 to calculate an inversion of the map  $\bar{\mathcal{M}}$  in a given point. Gradient descent is  
 775 an iterative minimization algorithm for multivariate functions. Let  $R \in \mathcal{R}$  be  
 776 a point in the readout space; we want to find a point  $D = (x, y, z) \in \mathcal{D}$  in  
 777 the detector space such that

$$\bar{\mathcal{M}}(D) = R = (x'_R, y'_R, t_R). \quad (3.13)$$

778 We define a function  $f_R$  in the readout space as a distance in this space:

$$f_R(x', y', t) = \sqrt{(x' - x'_R)^2 + (y' - y'_R)^2 + v_d^2(t - t_R)^2}, \quad (3.14)$$

779 where  $v_d$  is an approximation of the drift velocity in the TPC, obtained from  
780 the reconstruction in Section 3.1 (there will be an image with the linear fit here).

781 We make an initial guess (actually in the original code we just take  $z = 0$ ):

$$D_0 = (x'_R, y'_R, v_d t). \quad (3.15)$$

782 Assuming we have the  $n$ -th estimate  $D_n$ , we calculate the  $i$ -th component of  
783 the gradient of  $f_R \circ \bar{\mathcal{M}}$  numerically using central differences: (signs look correct)

$$[\nabla(f_R \circ \bar{\mathcal{M}})]^i(D_n) \approx \frac{f_R(\bar{\mathcal{M}}(D_n + s \cdot e^i)) - f_R(\bar{\mathcal{M}}(D_n - s \cdot e^i))}{2s}, \quad (3.16)$$

784 where  $e^i \in \mathcal{D}$  is the  $i$ -th coordinate vector and  $s$  is the step size. The step size  
785 should be sufficiently small; initially, we set it as a fraction  $s = \frac{l}{10}$  of the map's  
786 grid spacing  $l$ . During the minimization, we check that  $f_R(\bar{\mathcal{M}}(D_n)) < 10s$  at all  
787 times (s can (?) change – check). When using trilinear interpolation, it would be  
788 more efficient to calculate the gradient explicitly ( $\pm$  same result). This could be  
789 implemented inside the *Field* template class. The next iteration can be calculated  
790 as follows:

$$D_{n+1} = D_n - \gamma \nabla(f_R \circ \bar{\mathcal{M}})(D_n), \quad (3.17)$$

791 where  $\gamma \in \mathbb{R}^+$  is the damping coefficient. It should be set to a small enough  
792 value to ensure convergence, but large enough for sufficient converging speed.  
793 The minimization stops either when the error  $f_R(\bar{\mathcal{M}}(D_n))$  drops below a specified  
794 value or when the number of iterations exceeds a certain limit (in this case,  
795 a message is printed into the console). The parameters of this method can be  
796 further optimized (e.g., a better choice of  $\gamma$ , gradient computation); instead, we  
797 later decided to use the interpolation on the inverse grid described in the next  
798 section.

799 Measure reconstruction duration and compare it with the inverse grid inter-  
800 polation? Also compare the result? Typical evolution of  $D_n$  during search. Not  
801 sure if this has to be cited.

### 802 3.2.2 Interpolation on the Inverse Grid

803 Interpolation should be generally faster than the gradient descent since we don't  
804 need to iterate. We also don't need to optimize it to improve performance, if  
805 it's too slow we can even calculate the coefficients for the entire map before  
806 reconstruction (again, do some profiling).

807 The best current algorithm uses the interpolation on the inverse grid. Rather  
808 than inverting the trilinearly interpolated map using a numerical minimization  
809 method as in the previous section, we take advantage of the fact that the map  
810  $\bar{\mathcal{M}}$  is one-to-one (isomorphism is supposed to preserve structure, not sure how  
811 to interpret that here, not the best description, we already (kind of) assume it  
812 is a bijection by saying we will invert it). Since we have simulated values of this  
813 map on a regular grid in the detector space  $\mathcal{D}$ , we also know the inverse map  $\bar{\mathcal{M}}^{-1}$

814 on the irregular inverse grid in the readout space  $\mathcal{R}$ . To get an approximation  
 815 of the inverse map in the entire readout space, we can use interpolation (**general**  
 816 **concept, the specific choice is described below**).

817 Since the inverse grid is irregular, trilinear interpolation cannot be applied.  
 818 Given that the simulated map is dense enough to provide a good approximation  
 819 considering the size of our pads, we can adopt a similar approach.<sup>2</sup> As shown in  
 820 Equation 1.21 in Section 1.4.3, trilinear interpolation (**shouldn't need an article**  
 821 **when talking about a general concept**) can be expressed as a polynomial:

$$\hat{f}(x, y, z) = axyz + bxy + cxz + dyz + ex + fy + gz + h, \quad (3.18)$$

822 where  $a, b, c, d, e, f, g, h$  are coefficients uniquely determined by the values of  
 823 the function at the vertices of the interpolation cell (**can be calculated in the**  
 824 **way shown in the mentioned equation, not sure what more to add**). We can gen-  
 825 eralize this for a function defined on an irregular grid. Given the function values  
 826 at any eight points, we can write a system of eight linear equations

$$\begin{pmatrix} x_1y_1z_1 & x_1y_1 & x_1z_1 & y_1z_1 & x_1 & y_1 & z_1 & 1 \\ \vdots & \vdots \\ x_8y_8z_8 & x_8y_8 & x_8z_8 & y_8z_8 & x_8 & y_8 & z_8 & 1 \end{pmatrix} \begin{pmatrix} a \\ \vdots \\ h \end{pmatrix} = \begin{pmatrix} f(x_1, y_1, z_1) \\ \vdots \\ f(x_8, y_8, z_8) \end{pmatrix}, \quad (3.19)$$

827 which has a unique solution for the coefficients for most values of  $(x_n, y_n, z_n)$  and  
 828  $f(x_n, y_n, z_n)$ , where  $n \in \{1, \dots, 8\}$ .

829 This approach introduces a small complication: finding the correct pseudo-  
 830 cell (i.e., the image of eight vertices forming a cubic cell in the regular grid) in  
 831 the inverse grid. The eight irregularly spaced vertices of this pseudocell do not  
 832 define a unique volume, so there are multiple possible ways to partition  $\mathcal{R}$  into  
 833 pseudocells, with no obvious choice among them.

834 We are currently ignoring this problem and performing binary search along  
 835  $x, y, z$  (in this order). It shouldn't matter too much because the 70/30 map  
 836 doesn't cause such a big distortion and was even accidentally extrapolated for all  
 837  $z$  different from the central plane.

---

<sup>2</sup>A more complicated and computationally heavy alternative would be natural neighbor interpolation or Kriging.

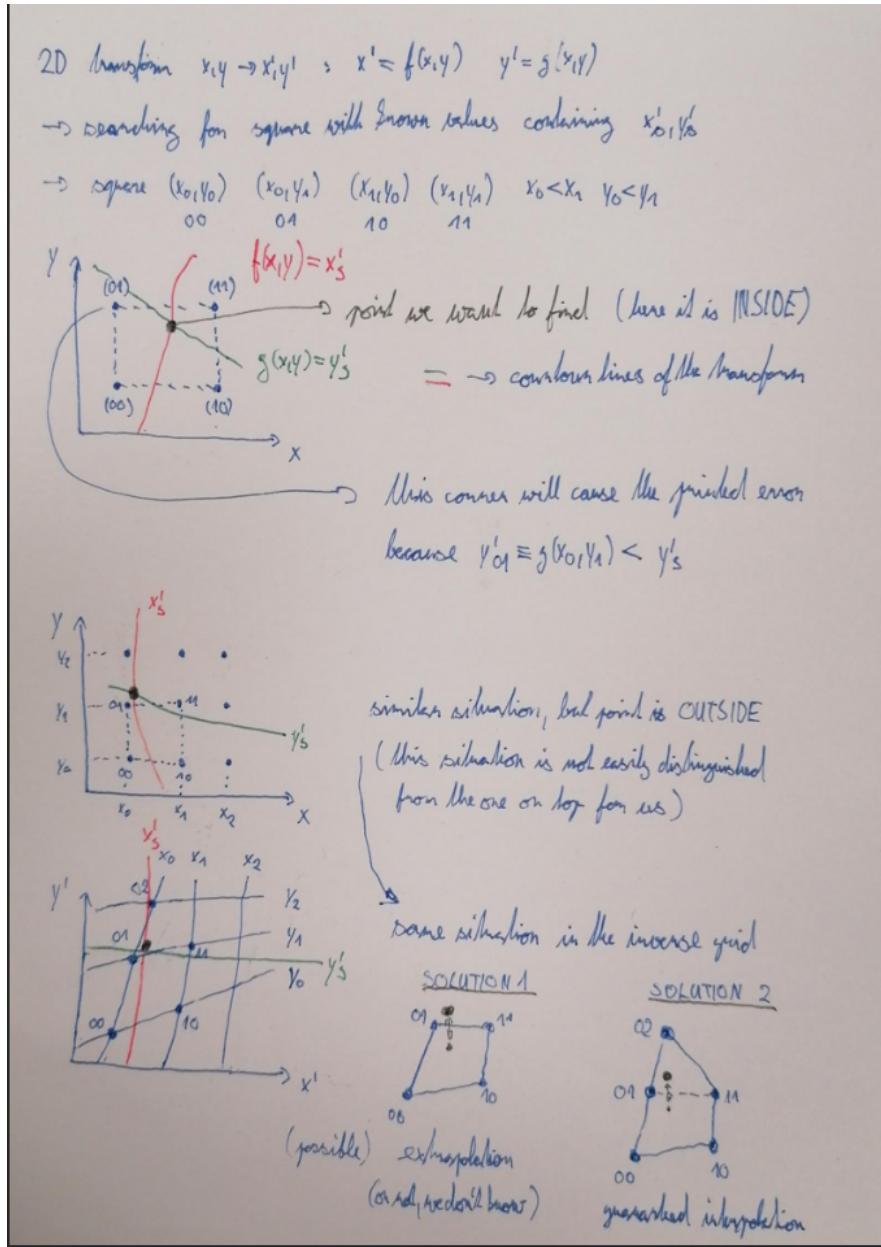


Figure 3.12: Selection of the points for interpolation. Create better images; use the explanation interpolation vs. extrapolation strange property. Solution 2 probably does not make much sense.

### 3.3 Discrete Reconstruction

838 Reconstruction with pads and time bins. Maybe testing different pads.

840 It is also possible to make this a subsection of the map, making the previous  
841 subsections parts of a new subsection 'Map Inversion'.

842 In order to get a more realistic representation of a track measured in the OFTPC,  
843 we need to take the discretization of the position and time data into account.  
844 The readout of the OFTPC will consist of 128 pads, their layout is shown in  
845 Fig. 1.7. Time is read out in discrete bins of size  $t_{\text{bin}} = 100$  ns.

846 As the first approximation, we can neglect the multiplication in the triple-GEM.

and assume an ideal charge readout. The time measurement starts at the beginning of the electron/positron simulation (depending on the specific simulation it can correspond to the production in the target or when entering the OFTPC, here the specific time doesn't matter too much since the primary particle travels basically at light speed (30 ps/cm) which is circa immediate given the time binning). Randomize this time a bit and see what it does to the reconstruction. The readout coordinates  $(x', y', t) \in \mathcal{R}$  of each ionization electron can be mapped to the pad coordinates  $(n_{\text{pad}}, n_t) \in \mathcal{P}$ :

$$n_{\text{pad}} = n: (x', y') \in \left[ x_{1,n} - \frac{g}{2}, x_{2,n} + \frac{g}{2} \right] \times \left[ y_{1,n} - \frac{g}{2}, y_{2,n} + \frac{g}{2} \right], \quad (3.20)$$

$$n_t = \left\lceil \frac{t}{t_{\text{bin}}} \right\rceil, \quad (3.21)$$

where  $x, y_{1,n}$  and  $x, y_{2,n}$  are the opposing pad corner coordinates, and  $g$  is the gap between the pads (described in detail in Section 1.4.2). This way, the closest pad is assigned to each readout position within the OFTPC volume<sup>3</sup>. Makes sense since the pads attract the electrons, the inhomogeneity of electric field is neglected. The number of electrons collected by each pad (i.e., collected charge) in each time bin is then counted and serves as a weight for the energy reconstruction. The reconstructed track consists of points for each  $(n, n_t) \in \mathcal{P}$ , we get these by reconstructing the position of a hypothetical electron with the readout coordinates of the pad/time bin center.<sup>4</sup>

$$\mathcal{D} \ni (x, y, z) = \overline{\mathcal{M}} \left( x_{c,n}, y_{c,n}, \left( n_t - \frac{1}{2} \right) t_{\text{bin}} \right). \quad (3.22)$$

---

<sup>3</sup>Some positions near the wall are not handled and some pads extend beyond the OFTPC volume. This is where an electric field simulation would come in handy.

<sup>4</sup>Mapping the center of the pad (along with the midpoint of the time bin) isn't necessarily the best approach since it might not correspond to the average parameters of an electron with these readout parameters.

## 864 4. Energy Reconstruction

865 The second stage is the reconstruction of the particle's energy using a fit of its  
866 reconstructed track (see Section 3). We have tested three ways of reconstructing  
867 the energy. Fitting is done using the MINUIT algorithm implemented in  
868 ROOT [2]. Cite some CERN article directly on MINUIT, can add a section. Or  
869 is it done using MIGRAD? The circle and RK4 probably was.

870 The **Cubic Spline Fit** was a tested and later rejected method of energy reconstruction.  
871 It uses smoothly connected piecewise cubic polynomials between uniformly spaced nodes.  
872 The reconstructed energy is calculated using the fit parameters by computing the radius of curvature in different points of the fitted  
873 curve using the known magnitude of the magnetic field perpendicular to the trajectory.  
874 We rejected this method because the tuning of the fit turned out to be unpractical compared to the other used methods. Reconstructs energy at every  
875 position (even though the actual energy doesn't change much) and it might be slower but no profiling has been done yet. Of course, it wasn't tested on the  
876 newer track reconstruction methods at all.

877 The **Circle and Lines Fit** was chosen as an alternative since this corresponds to the shape of a trajectory of a charged particle crossing a finite volume  
878 with a homogeneous magnetic field. The energy of the particle can be estimated  
879 using the fitted radius and the magnitude of the perpendicular magnetic field in the middle of the TPC.

880 The **Runge-Kutta Fit** uses the 4th order Runge-Kutta numerical integration described in Section 2.2. Initial parameters of the track (including the particle's energy) are optimized so that the integrated trajectory fits to the reconstructed one. This fit can also be performed as a single parameter (i.e., energy) fit if we get the initial position and orientation of the particle on the entrance to the TPC from previous detectors (TPX3 and MWPC, see Section 0.2).

### 891 4.1 Cubic Spline Fit

892 The first method for the estimation of the kinetic energy of the particle uses  
893 a cubic spline fit. We use an electron track simulated using the microscopic

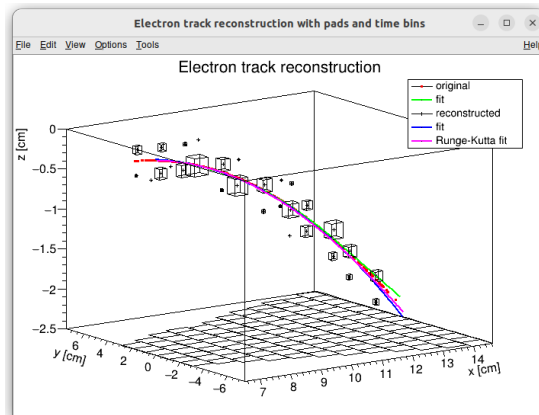


Figure 4.1: Example of a fitted reconstructed track. Swap for better image.

simulation, described in detail in Section 2.1.1. The track was reconstructed using the map described in Section 3.2.

In order to calculate the spline, we use the class *TSplines3* from ROOT. This allows us to evaluate the spline using the coordinates  $(x_n, z_n)$  of each node and the derivatives  $d_1, d_2$  in the first and the last node. We can fit these parameters of a fixed amount of nodes to the simulated trajectory. We use the IMPROVE algorithm provided by the *TMinuit* class in ROOT (there are some guidelines for fonts in MFF UK template (Czech version) that I will eventually apply (see notes in the conclusion)). This algorithm attempts to find a better local minimum after converging (could reformulate a bit, taken word for word from some manual).

After the fit converges, we calculate an energy estimate using the radius of curvature, which we can extract from the fitted spline equation at every point of the trajectory. The part of the spline corresponding to a given node is defined as

$$z(x) = z_n + b\Delta x + c(\Delta x)^2 + d(\Delta x)^3, \quad (4.1)$$

where  $\Delta x = x - x_n$  and  $b, c, d$  are coefficients. Using this equation, we derive the radius of curvature<sup>1</sup> as:

$$r(x) = \frac{(1 + z'^2(x))^{\frac{3}{2}}}{z''(x)} = \frac{(1 + (b + 2c\Delta x + 3d(\Delta x)^2)^2)^{\frac{3}{2}}}{2c + 6d\Delta x}. \quad (4.2)$$

Based on the geometry of our detector, we assume that the magnetic field satisfies  $\mathbf{B}(x, 0, z) = (0, B(x, z), 0)$  for a track in the XZ plane. Since the electron is relativistic, the effect of the electric field on its trajectory is negligible. The Lorentz force  $F_L$  is then always perpendicular to the momentum of the electron and acts as a centripetal force  $F_c$  (not quite sure how to handle this then?):

$$\begin{aligned} \mathbf{F}_L &= \mathbf{F}_c, \\ \|e\mathbf{v} \times \mathbf{B}\| &= \frac{\gamma m_e v^2}{r}, \\ ec\beta B &= \frac{E_{0e}\beta^2}{r\sqrt{1 - \beta^2}}, \\ \sqrt{1 - \beta^2} &= \frac{E_{0e}\beta}{ecBr}, \end{aligned} \quad (4.3)$$

$$\beta^2(x) = \left[ 1 + \left( \frac{E_{0e}}{ecB(x, z(x))r(x)} \right)^2 \right]^{-1}, \quad (4.4)$$

where  $e$  is the elementary charge,  $c$  is the speed of light in vacuum,  $m_e$  is the rest mass of electron,  $E_{0e} = m_e c^2$  is its rest energy,  $\gamma$  is the Lorentz factor,  $\mathbf{v}$  is the velocity of the electron, and  $\beta = \frac{v}{c}$ . The kinetic energy for a given point on the trajectory is then given as

$$E_{\text{kin}}(x) = \left( \frac{1}{\sqrt{1 - \beta^2(x)}} - 1 \right) E_{0e}. \quad (4.5)$$

---

<sup>1</sup>For the general formula see [https://en.wikipedia.org/wiki/Curvature#Graph\\_of\\_a\\_function](https://en.wikipedia.org/wiki/Curvature#Graph_of_a_function).

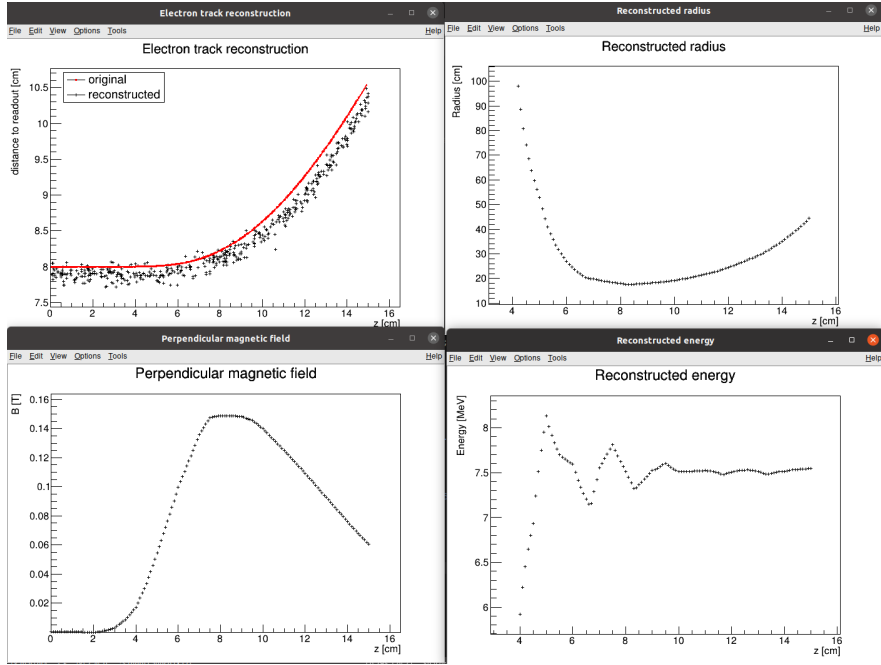


Figure 4.2: First attempt at a track reconstruction using only the drift velocity. Spline energy reconstruction attempt. Swap for better image(s) – subfigure environment, correct coordinates.

918 We can then average these estimates at multiple points (possibly using some  
 919 weights to account for the change in accuracy, this wasn't optimized and we just  
 920 ended with the graph) to get a single value. This method was later rejected in  
 921 favor of the circle and lines fit (the name was already established at the beginning  
 922 of the chapter) described in the next section. Add some figures.

## 923 4.2 Circle and Lines Fit

924 Another way to estimate the particle's kinetic energy is to fit its (??) trajectory  
 925 with a circular arc with lines attached smoothly. This shape of trajectory cor-  
 926 responds to a movement of a charged particle through a homogeneous magnetic  
 927 field perpendicular to the particle's momentum and limited to a certain volume.  
 928 In general, the shape of such a trajectory with a non-perpendicularly oriented  
 929 momentum is a spiral. In our case, the magnetic field is approximately toroidal  
 930 and the particle motion is nearly perpendicular to it (verify, could add some  
 931 magnetic field plots in different vertical planes; shouldn't have a big effect on the  
 932 reconstructed radius anyway). At first, we tested a 2D version of this fit, then  
 933 we adapted it to 3D.

934 The field in our detector is not homogeneous, it is therefore not entirely clear  
 935 what value of magnetic field should be used along with the fitted radius (using  
 936 equations 4.4 and 4.5) to get the best estimate for the kinetic energy. Since we  
 937 only use this method as the first iteration of the particle's energy that we later  
 938 refine, an optimal solution of this problem is not required. Instead, we tested two  
 939 options: taking the value of the field in the middle of the fitted circular arc (or  
 940 is it in the middle  $x$  of the OFTPC?) and taking the average field along it. We

haven't really tried to plot this for multiple tracks, but these estimates are saved somewhere and could be plotted.

### 4.2.1 Two-dimensional fit

In the 2D case, the fitted function used for the electron track<sup>2</sup> described in Section 2.1.1 (one specific track at the time, technically this function doesn't work for a curvature that gets outside of the semicircle) is defined as follows:

$$z(x) = \begin{cases} a_1x + b_1 & x < x_1 \\ z_0 + \sqrt{r^2 - (x - x_0)^2} & x_1 \leq x \leq x_2 \\ a_2x + b_2 & x > x_2 \end{cases}, \quad (4.6)$$

where  $a_{1,2}$  and  $b_{1,2}$  are the parameters of the lines,  $(x_0, z_0)$  is the center of the circle,  $r$  is its radius, and  $(x_{1,2}, z_{1,2})$  are the coordinates of the function's nodes. That means we have 9 parameters ( $z_{1,2}$  are not used in the function) along with 2 continuity conditions and 2 smoothness conditions (9 parameters of the described function, 5 of them independent after taking the conditions into account). For the fit, we use the coordinates of the nodes and the radius of the circle, which gives us 5 independent parameters (only the radius has to be larger than half of the distance between nodes). The continuity conditions (combined with the relations for  $z_{1,2}$ ) are

$$z_{1,2} = a_{1,2}x_{1,2} + b_{1,2} = z_0 - \sqrt{r^2 - (x_{1,2} - x_0)^2}, \quad (4.7)$$

the smoothness conditions are

$$a_{1,2} = \frac{x_0 - x_{1,2}}{\sqrt{r^2 - (x_{1,2} - x_0)^2}}. \quad (4.8)$$

Together with the Equation 4.7 we get the values of  $b_{1,2}$

$$b_{1,2} = z_{1,2} - a_{1,2}x_{1,2}. \quad (4.9)$$

For the coordinates of the center of the circle, we can use the fact that the center has to lie on the axis of its chord. In other words, there is a value of a parameter  $t$  such that, using the parametric equation of the axis

$$\begin{pmatrix} x_0 \\ z_0 \end{pmatrix} = \begin{pmatrix} \frac{x_1+x_2}{2} \\ \frac{z_1+z_2}{2} \end{pmatrix} + t \begin{pmatrix} \frac{z_2-z_1}{2} \\ \frac{x_1-x_2}{2} \end{pmatrix}. \quad (4.10)$$

At the same time, the center has to be in a distance of  $r$  from the nodes:

$$\begin{aligned} (x_1 - x_0)^2 + (z_1 - z_0)^2 &= r^2, \\ \left( \frac{x_1 - x_2}{2} + \frac{z_1 - z_2}{2}t \right)^2 + \left( \frac{z_1 - z_2}{2} + \frac{x_2 - x_1}{2}t \right)^2 &= r^2, \\ \left( \left( \frac{x_2 - x_1}{2} \right)^2 + \left( \frac{z_2 - z_1}{2} \right)^2 \right)t^2 + \left( \frac{x_2 - x_1}{2} \right)^2 + \left( \frac{z_2 - z_1}{2} \right)^2 - r^2 &= 0. \end{aligned} \quad (4.11)$$

---

<sup>2</sup>Electron tracks bend towards negative  $z$ , we need to use the upper part of the circle.

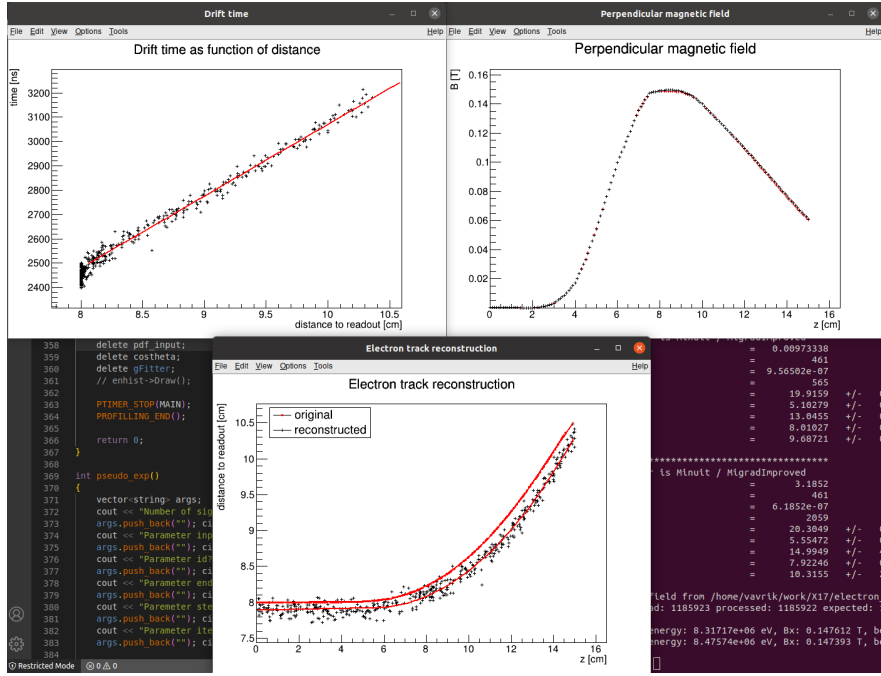


Figure 4.3: First attempt at a track reconstruction using only the drift velocity. Circle and Lines Fit in 2D. Swap for better image, correct coordinates. Bias should be described in the previous chapter, not here.

962 Since our electron track bends towards negative  $z$  and  $x_2 > x_1$ , we only care  
963 about the solution with  $t > 0$

$$t = \sqrt{\frac{r^2}{\left(\frac{x_2-x_1}{2}\right)^2 + \left(\frac{z_2-z_1}{2}\right)^2} - 1}, \quad (4.12)$$

$$x_0 = \frac{x_1 + x_2}{2} + \frac{z_2 - z_1}{2} \sqrt{\frac{r^2}{\left(\frac{x_2-x_1}{2}\right)^2 + \left(\frac{z_2-z_1}{2}\right)^2} - 1}, \quad (4.13)$$

$$z_0 = \frac{z_1 + z_2}{2} - \frac{x_2 - x_1}{2} \sqrt{\frac{r^2}{\left(\frac{x_2-x_1}{2}\right)^2 + \left(\frac{z_2-z_1}{2}\right)^2} - 1}.$$

964 The function defined in Equation 4.6 along with equations 4.8, 4.9, and 4.13  
965 derived using the continuity and smoothness conditions (combined with the re-  
966 lations for  $z_{1,2}$ ) fully define our fitted function with parameters  $r, x_{1,2}, z_{1,2}$ . Some  
967 pictures of the fit on the tested track. Results of the fit. Again, the actual fit  
968 uses 8-z. Use GeoGebra schematics to generate a picture of 2D geometry.

### 969 4.2.2 Three-dimensional fit

970 In three dimensions, the shape of a trajectory of a charged particle in a uniform  
971 magnetic field is a cylindrical helix. Nevertheless, since we assume that the  
972 field is approximately perpendicular to the particle's momentum at all times,  
973 we will further approximate the trajectory with a circular arc  $\mathbf{X}_C(\phi)$  (with lines  
974  $\mathbf{X}_{L1}(t), \mathbf{X}_{L2}(s)$  attached smoothly).

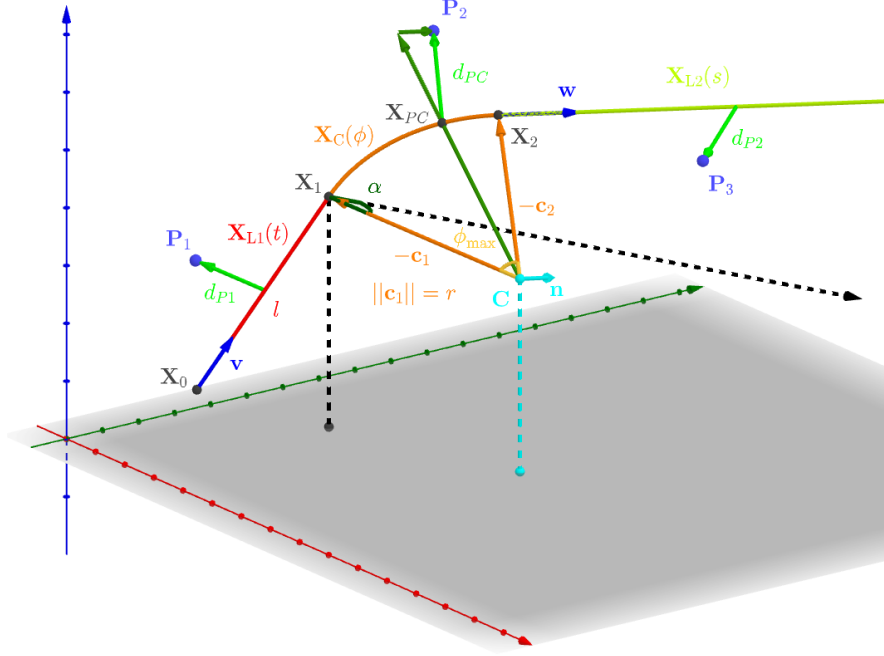


Figure 4.4: Visualization of the 3D geometry of the Circle and Lines Fit and its parameters.

We assume that the initial position  $\mathbf{X}_0 = (x_0, y_0, z_0)$  and direction  $\theta, \varphi$  (spherical angles as in Section 1.4.2) are known, since this information will be provided by TPX3 and MWPC layers. We could further refine it at the end of the current algorithm with some kind of global fit (all detector layers). The fit then has four free parameters (see Fig. 4.4):

- the length of the first line  $l$  (as measured from the initial position),
- the radius of the circular arc  $r$ ,
- the central angle of the arc  $\phi_{\max} \in [0, 2\pi]$ ,
- the direction of the curvature given by the angle  $\alpha \in [0, 2\pi]$  (right-handed with respect to the particle direction,  $\alpha = 0$  if the particle curves towards negative  $z$  in a plane given by  $\hat{\mathbf{z}}$  and the direction vector).

Using these parameters, we can derive a parametrization of the whole curve. Let  $\mathbf{v}$  be the initial unit direction vector, i.e., using the spherical angles

$$\mathbf{v} = (\cos \varphi \cos \theta, \sin \varphi \cos \theta, \sin \theta)^T, \quad (4.14)$$

then we can parameterize the first line as follows:

$$\mathbf{X}_{L1}(t) = \mathbf{X}_0 + t\mathbf{v} \quad t \in [0, l]. \quad (4.15)$$

This gives us the starting point of the arc

$$\mathbf{X}_1 = \mathbf{X}_{L1}(l) = \mathbf{X}_0 + l\mathbf{v}. \quad (4.16)$$

The vector  $\mathbf{c}_1$  that lies in the plane of curvature and points from  $\mathbf{X}_1$  to the center of curvature can be calculated using a composition of rotations. First, we rotate  $\mathbf{v}$  to point in the  $\hat{\mathbf{x}}$  direction, the normal for  $\alpha = 0$  than points in the  $-\hat{\mathbf{z}}$  direction,

993 we apply the  $\alpha$  rotation and reverse the rotations into the  $\hat{\mathbf{x}}$  direction: (parameters  
994 are explained in the bullet points above)

$$\begin{aligned}
\mathbf{c}_1 &= R_z(\varphi)R_y(-\theta)R_x(\alpha)R_y\left(\frac{\pi}{2}\right)R_y(\theta)R_z(-\varphi)\mathbf{v}, \\
&= R_z(\varphi)R_y(-\theta)R_x(\alpha)(-\hat{\mathbf{z}}), \\
&= \begin{pmatrix} \cos \varphi & -\sin \varphi & 0 \\ \sin \varphi & \cos \varphi & 0 \\ 0 & 0 & 1 \end{pmatrix} \begin{pmatrix} \cos \theta & 0 & -\sin \theta \\ 0 & 1 & 0 \\ \sin \theta & 0 & \cos \theta \end{pmatrix} \begin{pmatrix} 1 & 0 & 0 \\ 0 & \cos \alpha & -\sin \alpha \\ 0 & \sin \alpha & \cos \alpha \end{pmatrix} \begin{pmatrix} 0 \\ 0 \\ -1 \end{pmatrix}, \quad (4.17) \\
&= \begin{pmatrix} -\sin \alpha \sin \varphi + \cos \alpha \cos \varphi \sin \theta \\ \sin \alpha \cos \varphi + \cos \alpha \sin \varphi \sin \theta \\ -\cos \alpha \cos \theta \end{pmatrix}.
\end{aligned}$$

995 Signs should be correct because right-handed rotation around  $y$  rotates  $z$  into  $x$   
996 and this one is the opposite. Seems like in this part of the code  $\theta$  is actually taken  
997 from the pole. Instead of the equator plane. Similarly by rotating  $\hat{\mathbf{y}}$ , we can get  
998 the normal vector  $\mathbf{n} = \mathbf{v} \times \mathbf{c}_1$  perpendicular to the plane of the trajectory:

$$\mathbf{n} = R_z(\varphi)R_y(-\theta)R_x(\alpha)\hat{\mathbf{y}} = \begin{pmatrix} -\cos \alpha \sin \varphi - \sin \alpha \cos \varphi \sin \theta \\ \cos \alpha \cos \varphi - \sin \alpha \sin \varphi \sin \theta \\ \sin \alpha \cos \theta \end{pmatrix}. \quad (4.18)$$

999 This allows us to express the coordinates of the center  $\mathbf{C}$  of the circular arc:

$$\mathbf{C} = \mathbf{X}_1 + r\mathbf{c}_1. \quad (4.19)$$

1000 We can then get the parametrization and the endpoint of the circular arc using  
1001 Rodrigues' rotation formula: (all parameters explained in the bullet points above)

$$\begin{aligned}
\mathbf{c}_2 &= \mathbf{c}_1 \cos \phi_{\max} + (\mathbf{n} \times \mathbf{c}_1) \sin \phi_{\max} + \mathbf{n}(\mathbf{n} \cdot \mathbf{c}_1)(1 - \cos \phi_{\max}), \\
&= \mathbf{c}_1 \cos \phi_{\max} - \mathbf{v} \sin \phi_{\max},
\end{aligned} \quad (4.20)$$

$$\mathbf{X}_C(\phi) = \mathbf{C} - r(\mathbf{c}_1 \cos \phi - \mathbf{v} \sin \phi) \quad \phi \in [0, \phi_{\max}], \quad (4.21)$$

$$\mathbf{X}_2 = \mathbf{X}_C(\phi_{\max}) = \mathbf{C} - r\mathbf{c}_2, \quad (4.22)$$

1002 and if we define the direction vector of the second line, we also get its parametriza-  
1003 tion

$$\mathbf{w} = \mathbf{v} \cos \phi_{\max} + (\mathbf{n} \times \mathbf{v}) \sin \phi_{\max} = \mathbf{v} \cos \phi_{\max} + \mathbf{c}_1 \sin \phi_{\max}, \quad (4.23)$$

$$\mathbf{X}_{L2}(s) = \mathbf{X}_2 + s\mathbf{w} \quad s \in [0, \infty). \quad (4.24)$$

1004 The fit is performed as a (weighted) least square minimization (**MIGRAD**  
1005 **ROOT**), therefore we need to derive the distance of any point  $\mathbf{P}$  to the fitted  
1006 curve. For the first line, we simply compute the parameter value of the closest  
1007 point on the line:

$$\begin{aligned}
t_P &= \mathbf{v} \cdot (\mathbf{P} - \mathbf{X}_1), \\
d_{P1} &= \|\mathbf{P} - \mathbf{X}_{L1}(t_P)\|.
\end{aligned} \quad (4.25)$$

1008 If the parameter value is outside of its bounds defined above, we take the bound-  
1009 ary value instead. The distance to the second line is computed likewise. For

1010 the circular arc ([specific circular arc in the fit](#)), we find the closest point ([on the](#)  
 1011 [arc](#)) by projecting the center connecting line onto the arc plane:

$$\mathbf{X}_{PC} = \mathbf{C} + r \frac{(\mathbf{P} - \mathbf{C}) - (\mathbf{n} \cdot (\mathbf{P} - \mathbf{C}))\mathbf{n}}{\|(\mathbf{P} - \mathbf{C}) - (\mathbf{n} \cdot (\mathbf{P} - \mathbf{C}))\mathbf{n}\|}, \quad (4.26)$$

$$d_{PC} = \|\mathbf{P} - \mathbf{X}_{PC}\| \quad (4.27)$$

1012 If the point  $\mathbf{X}_{PC}$  lies outside of the arc, distance to the closest endpoint is taken  
 1013 instead. The shortest distance out of  $d_{P1}, d_{PC}, d_{P2}$  is then taken as the distance  
 1014 to the curve. When calculating energy with the average field, only the arc is  
 1015 considered. Middle field in the current implementation taken in the middle  $x$   
 1016 plane (intersection with the curve). TVirtualFitter+MIGRAD, maximal num of  
 1017 iterations, toleration. Different uncertainties in  $x, y, z$  not taken into account.

1018 Fit details (parameter bounds, initial setting).

### 1019 4.2.3 Testing on a Runge-Kutta sample

1020 The three dimensional circle and lines fit was tested on a sample of Runge-Kutta  
 1021 tracks with randomized parameters described in Section 2.2.1. These tracks of  
 1022 primary electrons and positrons consist of points calculated with the RK4 algo-  
 1023 rithm for a given proper time step ([step can be adjusted by dividing by the gamma](#)  
 1024 [factor → detector time](#)). Fitting with circle only was also partially implemented  
 1025 ([didn't work but could be fixed/tuned](#)).

## 1026 4.3 Runge-Kutta Fit

1027 The Runge-Kutta fit uses the Runge-Kutta 4th order (RK4) numerical integra-  
 1028 tion of the equation of motion (see Section 2.2) to find the best values of the track  
 1029 parameters – the track origin, initial velocity direction and the kinetic energy. In  
 1030 order to speed up the energy reconstruction, an initial guess of these parameters  
 1031 can be obtained from the 3D circle fit described in the previous section. Fur-  
 1032 thermore, assuming we know the track origin and orientation, we can perform  
 1033 a single parameter fit of the kinetic energy ([do some profiling and show that it is](#)  
 1034 [faster – below in the microscopic testing](#)).

1035 The fit is performed as a least square minimization of the (weighted) distances  
 1036 of the track points (true ionization vertices from the simulation or reconstructed  
 1037 points). The simulated RK4 track consists of line segments with known endpoints,  
 1038 therefore we can calculate the distance of a point from this segment analogically  
 1039 to Equation 4.25 with  $\mathbf{v}$  given as a unit vector in the direction of the segment.

1040 We need to find the segment with the lowest distance. We assume, that  
 1041 the distance  $d_{\mathbf{P}}(\tau)$  of a point  $\mathbf{P}$  to the point on the track (a curve parameterized  
 1042 by the proper time  $\tau$ )  $\mathbf{X}(\tau)$  has a single minimum (local and global), no local  
 1043 maximum (except the interval endpoints) and no saddle point

$$\exists! \tau_{\min} \in [0, \tau_N]: (\forall \tau \in [0, \tau_N]: d_{\mathbf{P}}(\tau) \geq d_{\mathbf{P}}(\tau_{\min})) \vee \frac{dd_{\mathbf{P}}}{d\tau}(\tau_{\min}) = 0, \quad (4.28)$$

1044 where  $N$  is the number of RK4 steps. This is a reasonable assumption for a track  
 1045 with an approximate shape of a circular arc with a radius  $r$ , since the distance  $d$

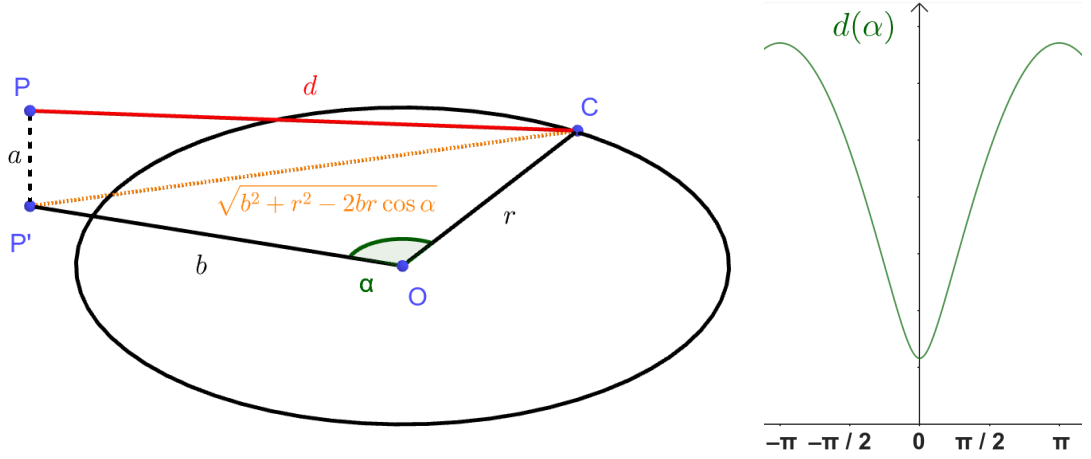


Figure 4.5: Demonstration of the convexity of the distance function  $d(\alpha)$  for a circular track (see Equation 4.29).

from a point **C** on the corresponding circle of a point **P** offset by  $a$  from the arc plane and by  $b$  from the arc's center when projected on its plane is given by the law of cosines:

$$d^2 = a^2 + b^2 + r^2 - 2br \cos \alpha, \quad (4.29)$$

where  $\alpha$  is the angle between points **C** and **P** as seen from the center of the arc (see Fig. 4.5). This function is strictly convex for  $\alpha \in (-\frac{\pi}{2}, \frac{\pi}{2})$  and in our case, the center of the arc lies outside of the detector and  $\alpha$  is restricted to a small interval around zero (especially considering that the initial guess should make the fitted trajectory reasonably close to any relevant point, in the worst-case scenario, the distance is overestimated which should keep the fit from converging to such solutions).

In a more general case, if we consider the vector  $\mathbf{a}(\tau) = \mathbf{P} - \mathbf{X}(\tau)$  whose size is  $\|\mathbf{a}(\tau)\| = d_{\mathbf{P}}(\tau)$ , then we get

$$2d_{\mathbf{P}} \frac{dd_{\mathbf{P}}}{d\tau} = \frac{dd_{\mathbf{P}}^2}{d\tau} = 2\mathbf{a} \cdot \frac{d\mathbf{a}}{d\tau} = -2\mathbf{a} \cdot \frac{d\mathbf{X}}{d\tau}, \quad (4.30)$$

therefore for the derivative of  $d_{\mathbf{P}}(\tau)$  to be zero,  $\mathbf{a}(\tau)$  has to be perpendicular to the tangent of the track. In 3D, for a given  $\mathbf{X}(\tau)$ , this condition restricts **P** to a plane. This means that on a curving track, for any two points  $\mathbf{X}(\tau_1), \mathbf{X}(\tau_2)$  with non-parallel tangents, we can find a point **P** that has  $\frac{dd_{\mathbf{P}}}{d\tau}(\tau_1) = \frac{dd_{\mathbf{P}}}{d\tau}(\tau_2) = 0$ , which violates the assumption 4.28. If we have a circle-and-lines track as described in the previous sections, such a point has to lie outside of the circular sector given by the arc.

For a planar track  $\mathbf{X}(\tau) = (X_1(\tau), X_2(\tau))$ , the envelope of all its normals is the evolute of the curve (i.e., the set of centers of all its osculating circles). If the track has a monotonous tangent angle

$$\alpha(\tau) = \text{atan} \frac{\frac{dX_2}{d\tau}}{\frac{dX_1}{d\tau}} \quad (4.31)$$

with minimal and maximal  $\alpha$  differing by less than  $\pi$  (i.e., the track changes direction by less than  $180^\circ$ ), then all intersections of the track's normals must lie

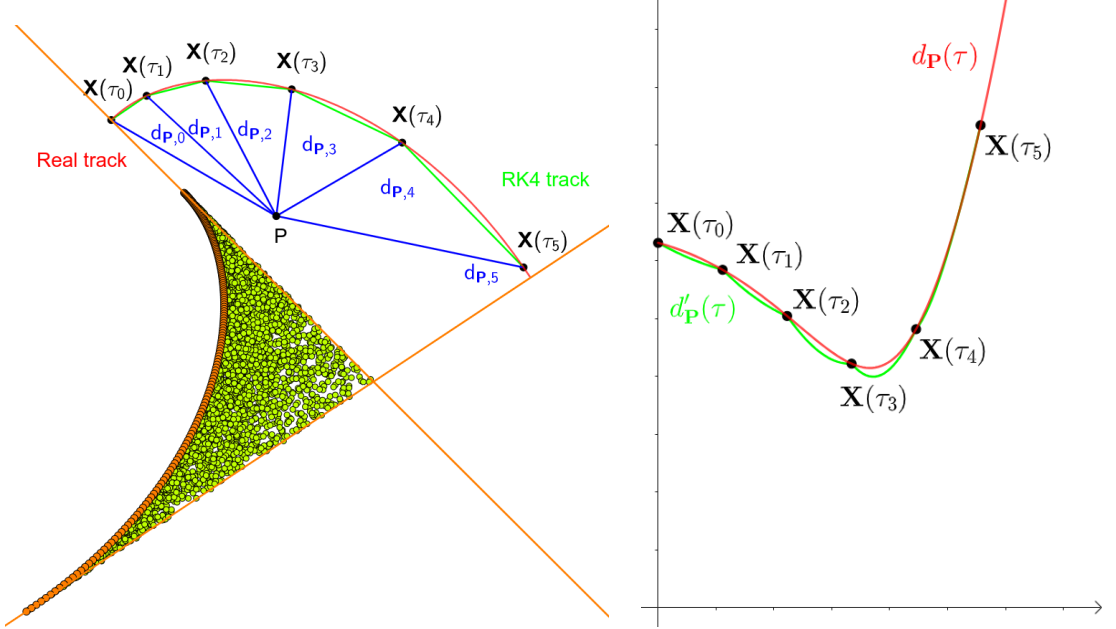


Figure 4.6: An example track (red) with a polygonal chain approximation (green, representing a RK4 simulation). The distance of the point  $\mathbf{P}$  from the chain is found using a binary search among the distances to the vertices  $d_{\mathbf{P}}(\tau_i)$  (blue) and subsequently calculating the distance to segments neighboring the found vertex (thus finding the minimum of the function  $d'_{\mathbf{P}}(\tau)$ , function  $d_{\mathbf{P}}(\tau)$  for the actual track is showed for reference). This approach works if the condition 4.28 is satisfied, which is not the case for a point from the green area bordered by the normals at endpoints and the evolute of the track (orange).

in an area bordered by the evolute and the normals at the beginning and the end of the curve (from their intersection with the evolute to their mutual intersection, see Figs. 4.6 and 4.7). Together, these three boundaries define a closed shape that will lie outside of the OFTPC for a typical track in our detector<sup>3</sup>.

With the assumption 4.28, we can find the segment on the RK4 track with the lowest distance to a given point  $\mathbf{P}$  using a binary search algorithm. Let the distance of the point from the  $n$ -th vertex be  $d_{\mathbf{P},n} = d_{\mathbf{P}}(\tau_n)$ . Then the difference  $\Delta d_{\mathbf{P},n} = d_{\mathbf{P},n} - d_{\mathbf{P},n-1}$  satisfies

$$\begin{aligned}\Delta d_{\mathbf{P},n} &< 0 \quad \forall n \text{ such that } \tau_n < \tau_{\min}, \\ \Delta d_{\mathbf{P},n} &> 0 \quad \forall n \text{ such that } \tau_{n-1} > \tau_{\min}.\end{aligned}\tag{4.32}$$

Therefore, we can search for the segment containing  $d_{\mathbf{P},\min} = d_{\mathbf{P}}(\tau_{\min})$  with binary search starting with  $\Delta d_{\mathbf{P},1}$  and  $\Delta d_{\mathbf{P},N}$ , then calculate the difference  $\Delta d_{\mathbf{P},m}$  for the middle index  $m = \left\lfloor \frac{N+1}{2} \right\rfloor$ . If  $\Delta d_{\mathbf{P},m} > 0$  (minor bug in the implementation – if the value for the maximal index is negative, it shouldn't change anything), we can replace the higher index with  $m$ , otherwise we replace the lower index. The search stops when the difference between the minimal and maximal index is one. Would it be better if they were the same (maybe not)? Then the minimal

---

<sup>3</sup>The smallest anticipated radius of curvature is 39 cm for an electron or positron with a kinetic energy 3 MeV in a 0.3 T magnetic field. All points in the exclusion area must be farther from the track and therefore outside the OFTPC.

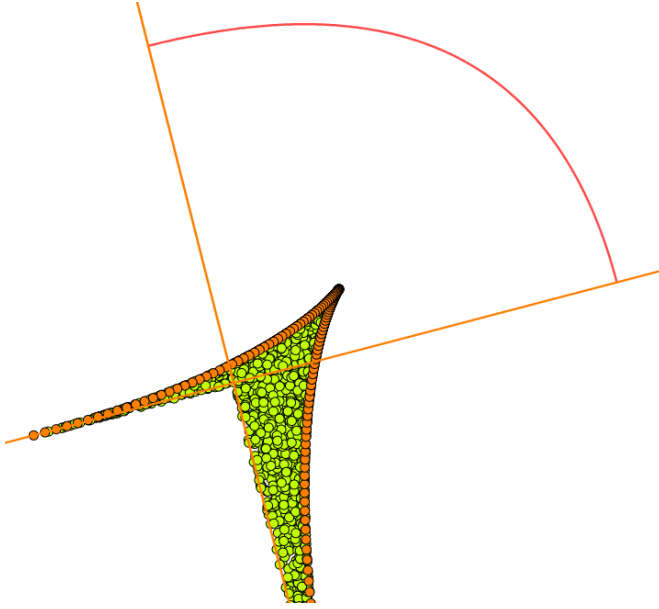


Figure 4.7: An exclusion area (green) of a track (red) bordered by its evolute and the normals at endpoints (orange), where the assumption 4.28 is violated. Unlike the track in Fig. 4.6, this track has a minimal curvature point in the middle, corresponding to the cusp on its evolute.

1085 value is  $d_{P,n-1}$  or  $d_{P,N}$  and we can take the minimum of the distances from the two  
 1086 segments connected to  $n - 1$ . Currently taking the maximal index (and starting  
 1087 at  $N - 2$  maximal index  $\leftrightarrow N - 1$ -th point), this should be equivalent, since either  
 1088  $\Delta d_{P,\max} > 0$  (in the code is equivalent to max-1 here) or we are at  $N - 1$ . The  
 1089 minimum of the two distances still taken.

1090 Same details with MIGRAD etc. as previously.

### 1091 4.3.1 Testing on a microscopic sample

1092 The Runge-Kutta fit together with the 3D circle-and-lines pre-fit was tested  
 1093 on a sample of tracks simulated using the microscopic simulation described in  
 1094 Section 2.1. At first, few tracks with randomized initial parameters (same as  
 1095 the Runge-Kutta sample in Section 2.2.1) were generated for preliminary testing.  
 1096 Later, a sample with a grid-like distribution of track parameters was generated  
 1097 (see Section 2.1.2 for details).

1098 Initial parameters of the HEED track (also should be in the first testing track).  
 1099 Initial parameters set in the circle fit (if electron set alpha one way, otherwise  
 1100 other way) and parameter bounds.

# 1101 Conclusion

1102 Here or at the end of each section. Something about the future of this work?

1103

## 1104 Notes

1105 General notes about the thesis:

- 1106 • Check that all of the classes and other code are marked the same way in
- 1107 the text. I used italics somewhere, could use different font for this instead.
- 1108 • Check unbreakable space in front of articles. Remove excessive article usage
- 1109 with proper nouns.
- 1110 • Currently using margins for single-sided printing (bigger on the left side).
- 1111 • Check that present tense is used
- 1112 • Active vs passive voice usage
- 1113 • American English quotation marks (") instead of British English (').
- 1114 • Some of the overfull hbox warnings might change if duplex printing is used
- 1115 (they generate black rectangles on the edge of the page), leaving them be
- 1116 for now
- 1117 • Check nobreakdash usage (is it always necessary)
- 1118 • Check capitalized references (e.g., Figure, Section, Equation)
- 1119 • Check  $\backslash(...\backslash)$  math mode instead of  $\$...$$ . (actually unlike  $\backslash[...\backslash]$  math mode,
- 1120 there is apparently no real benefit to this clumsy syntax)
- 1121 • Use siunitx package to ensure correct formatting, physics package for derivatives.
- 1122
- 1123 • Check other stuff that's written in the MFF UK template. Apparently it
- 1124 has since been updated and there are some differences (check for them).
- 1125 • Check correct subscripts in equation (italics vs no italics)
- 1126 • Consistent bold marking of points/vectors
- 1127 • Correct footnotes (capital letters, etc.).
- 1128 • Might have to mention GeoGebra as per the non-commercial license agree-
- 1129 ment (Made with GeoGebra®) – maybe put it into acknowledgments next
- 1130 to the MetaCentrum credit? And list all of the figures where GeoGebra was
- 1131 used?
- 1132 • Maybe make some section outside of References specifically for literature?
- 1133 (such as the old CERN TPC review, ATOMKI review is currently not
- 1134 mentioned, not sure if some Wikipedia articles should get a mention or how
- 1135 do these things work)
- 1136 • Consistent use of `bm` vs `mathbf`

- Consistent use of  $\bar{\mathcal{M}}$  instead of  $\mathcal{M}$  when talking about the map of the means (so most of the time)
  - Proper equation numbering when deriving a relation
  - Hugo should be mentioned somewhere in the title pages probably?
  - Consistent itemize/enumerate style (namely spacing) that looks good (ideally set by some macro? maybe the new MFF UK template will solve this?)
  - Consistent gas mixture notation (e.g., 90:10 Ar:CO<sub>2</sub>). Maybe mention at the beginning that it is a molar ratio.
  - Labels of figures and tables – maybe in bold? Abbreviated?
  - Check graph labels, make them bigger if needed.
  - "The map" can be viewed as a mapping between spaces or just as a coordinate transform.
  - Maybe switch to cleverref.
  - siunitx qty not SI
  - Correct em dash?
- Random notes:
- Terminology consistency – ionization/primary/secondary electrons
  - Consistent TPC vs OFTPC acronym usage in the text or individual chapters.
  - Only electrons that start and end in the sector closer than 0.5 cm are used for reconstruction (newest version).
  - Attachment, Penning transfer and secondary ionization not considered in the microscopic simulation.
  - Suspicious artifacts of trilinear interpolation in Fig. 1.8. **Fixed – integers instead of doubles in the implementation, influenced reconstruction SIGNIFICANTLY (but not simulation).**
  - Profiling of the reconstruction!!!! Find out what's taking the most time (probably Runge-Kutta integration which the fit calls a lot). Could gradually decrease the step size to refine the fit instead of making it small right away (arbitrarily small – the effect of this was never tested). This could take some time to do properly (find a profiler or make profiling macros).
  - Slow drift velocity good for  $z$  reconstruction, too low leads to recombination
  - Could add link to the GitHub repository, mention CMake? Details about simulating on MetaCentrum?
  - The first used track had 8 MeV momentum  $p = \gamma mv$  (not kinetic energy  $E_{\text{kin}} = (\gamma - 1)mc^2 = \sqrt{p^2c^2 + m^2c^4} - mc^2 \approx 7.5$  MeV)
  - Maybe cite Garfield++ user manual instead?
  - Using TRandom3 for random number generation.

- 1175     • Does the RK fit error correlate with the actual error?
- 1176     • Some Garfield settings in micro track generation probably not mentioned

## 1177 Future

1178 Things planned for the future:

- 1179     • Testing the reconstruction algorithm by measuring real particles with a known energy distribution.
- 1180
- 1181     • The **Fast Simulation with Ionization Electron Map** is planned for the future. It will use the HEED program [33] to simulate the primary particle and the Ionization Electron Map (see Section 3.2) to simulate the drift of secondary electrons. It should be significantly faster than the Microscopic Simulation but offer comparable precision since it will rely on an already simulated drift map. (Primary track simulated in HEED. Readout parameters by interpolating the map. Diffusion from the map for randomization.)
- 1182
- 1183
- 1184
- 1185
- 1186
- 1187
- 1188     • Account for GEM, delta electrons, ...
- 1189     • Likelihood approach instead of least squares (if it improves the reconstruction significantly), we should at least use a better method than taking the center of the TPC bin.
- 1190
- 1191
- 1192     • More detailed electric field simulation (if needed, GEM will have more complex field, some irregularities in the field should be considered)
- 1193
- 1194     • Account for the triggering in MWPC/TPX3 (particle travels from TPX3 to MWPC basically immediately – fraction of a nanosecond so there should be no significant difference)
- 1195
- 1196

1197

## 1198 Likelihood - inverse map

1199     If we wanted to further improve this procedure, taking into account the whole  
1200 map  $\mathcal{M}$ , we could make an "inverse map" from  $\mathcal{R}$  to distributions on  $\mathcal{D}$ . We could  
1201 achieve this by taking the normalized probability density of an electron with initial  
1202 coordinates  $(x, y, z)$  having readout coordinates  $(x', y', t)$ . If we fix  $(x', y', t)$ , we  
1203 get an unnormalized probability density  $f(x, y, z) = \mathcal{M}_{(x,y,z)}(x', y', t)$  (assuming  
1204 that all initial coordinates are a priori equally likely). This could potentially  
1205 improve the discrete reconstruction if we take the mean value of this probability  
1206 density across the pad and time bin

$$f_{\text{pad, bin}}(x, y, z) = \frac{1}{A_{\text{pad}} \Delta t_{\text{bin}}} \int_{\text{pad, bin}} \mathcal{M}_{(x,y,z)}(x', y', t) dx' dy' dt \quad (4.33)$$

1207     and using it for a likelihood fit instead of using least squares. This still assumes  
1208 that all initial coordinates are equally likely which is clearly not the case for  
1209 a primary particle track. In the future, we could even use the fast track simulation  
1210 with the map (should be possible to make around 1000 tracks per minute per core  
1211 with current settings), create a big set of tracks with reasonable parameters and

1212 use these to get an approximation of the probability distribution of the detector  
1213 response. Some approximations would be necessary when interpreting the data to  
1214 decrease the degrees of freedom of this distribution (we would have to pick a set of  
1215 parameters and assume that some of them are independent). This could give us  
1216 an idea about the best achievable resolution (how significantly will the detector  
1217 response differ for a given change in energy). If the difference is significant, we  
1218 could try to further improve the likelihood fit.

# Bibliography

1. *Garfield++* [<https://garfieldpp.web.cern.ch/garfieldpp/>]. [N.d.]. Accessed: 2023-05-18.
2. BRUN, Rene; RADEMAKERS, Fons. Root — An Object Oriented Data Analysis Framework. *Nucl. Instrum. Methods Phys. Res. Sect. A: Accel. Spectrom. Detect. Assoc. Equip.* 1997, vol. 389, no. 1–2, pp. 81–86. Available from DOI: 10.1016/s0168-9002(97)00048-x. Proceedings AIHENP'96 Workshop, Lausanne, Sep. 1996, See also <https://root.cern/>, Paper published in the Linux Journal, Issue 51, July 1998.
3. *About MetaCentrum* [<https://metavo.metacentrum.cz/en/about/index.html>]. 2023. Accessed: 2024-11-27.
4. ROSE, M. E. Internal Pair Formation. *Phys. Rev.* 1949, vol. 76, pp. 678–681. Available from DOI: 10.1103/PhysRev.76.678.
5. ESSIG, R. et al. *Dark Sectors and New, Light, Weakly-Coupled Particles*. 2013. Available from arXiv: 1311.0029 [hep-ph].
6. DE BOER, F.W.N. et al. A deviation in internal pair conversion. *Phys. Lett. B*. 1996, vol. 388, no. 2, pp. 235–240. ISSN 0370-2693. Available from DOI: [https://doi.org/10.1016/S0370-2693\(96\)01311-1](https://doi.org/10.1016/S0370-2693(96)01311-1).
7. BOER, F W N de et al. Excess in nuclear pairs near 9 MeV/ invariant mass. *J. Phys. G: Nucl. Part. Phys.* 1997, vol. 23, no. 11, p. L85. Available from DOI: 10.1088/0954-3899/23/11/001.
8. BOER, F W N de et al. Further search for a neutral boson with a mass around 9 MeV/c<sup>2</sup>. *J. Phys. G: Nucl. Part. Phys.* 2001, vol. 27, no. 4, p. L29. Available from DOI: 10.1088/0954-3899/27/4/102.
9. VITÉZ, Attila et al. Anomalous Internal Pair Creation in <sup>8</sup>Be as a Signature of the Decay of a New Particle. *Acta Phys. Pol. B - ACTA PHYS POL B*. 2008, vol. 39, p. 483.
10. KRASZNAHORKAY, A. et al. Searching for a light neutral axial-vector boson in isoscalar nuclear transitions. *Frascati Phys. Ser.* 2012, vol. 56, p. 86.
11. KRASZNAHORKAY, A. J. et al. Observation of Anomalous Internal Pair Creation in <sup>8</sup>Be: A Possible Indication of a Light, Neutral Boson. *Phys. Rev. Lett.* 2016, vol. 116, no. 4. ISSN 1079-7114. Available from DOI: 10.1103/physrevlett.116.042501.
12. TILLEY, D.R. et al. Energy levels of light nuclei A=8,9,10. *Nucl. Phys. A*. 2004, vol. 745, no. 3, pp. 155–362. ISSN 0375-9474. Available from DOI: <https://doi.org/10.1016/j.nuclphysa.2004.09.059>.
13. SAS, N. J. et al. *Observation of the X17 anomaly in the <sup>7</sup>Li(p,e<sup>+</sup>e<sup>-</sup>)<sup>8</sup>Be direct proton-capture reaction*. 2022. Available from arXiv: 2205.07744 [nucl-ex].
14. KRASZNAHORKAY, A. J. et al. New anomaly observed in <sup>4</sup>He supports the existence of the hypothetical X17 particle. *Phys. Rev. C*. 2021, vol. 104, no. 4. ISSN 2469-9993. Available from DOI: 10.1103/physrevc.104.044003.

- 1261 15. TILLEY, D.R. et al. Energy levels of light nuclei A = 4. *Nucl. Phys. A*.  
1262 1992, vol. 541, no. 1, pp. 1–104. ISSN 0375-9474. Available from DOI: [https://doi.org/10.1016/0375-9474\(92\)90635-W](https://doi.org/10.1016/0375-9474(92)90635-W).
- 1264 16. KRASZNAHORKAY, A. J. et al. New anomaly observed in  $^{12}\text{C}$  supports the  
1265 existence and the vector character of the hypothetical X17 boson. *Phys. Rev.*  
1266 *C*. 2022, vol. 106, p. L061601. Available from DOI: 10.1103/PhysRevC.106.  
1267 L061601.
- 1268 17. AJZENBERG-SELOVE, F. Energy levels of light nuclei A = 11,12. *Nucl. Phys.*  
1269 *A*. 1990, vol. 506, no. 1, pp. 1–158. ISSN 0375-9474. Available from DOI:  
1270 [https://doi.org/10.1016/0375-9474\(90\)90271-M](https://doi.org/10.1016/0375-9474(90)90271-M).
- 1271 18. KÁLMÁN, Péter; KESZTHELYI, Tamás. Anomalous internal pair creation.  
1272 *The Eur. Phys. J. A*. 2020, vol. 56. Available from DOI: 10.1140/epja/  
1273 s10050-020-00202-z.
- 1274 19. ALEKSEJEVS, A. et al. *A Standard Model Explanation for the "ATOMKI*  
1275 *Anomaly"*. 2021. Available from arXiv: 2102.01127 [hep-ph].
- 1276 20. FENG, Jonathan L. et al. Protophobic Fifth-Force Interpretation of the Ob-  
1277 served Anomaly in  $^8\text{Be}$  Nuclear Transitions. *Phys. Rev. Lett.* 2016, vol. 117,  
1278 p. 071803. Available from DOI: 10.1103/PhysRevLett.117.071803.
- 1279 21. ANH, Tran The et al. Checking the 8Be Anomaly with a Two-Arm Electron  
1280 Positron Pair Spectrometer. *Universe*. 2024, vol. 10, no. 4, p. 168. ISSN 2218-  
1281 1997. Available from DOI: 10.3390/universe10040168.
- 1282 22. ABRAAMYAN, Kh. U. et al. *Observation of structures at  $\sim 17$  and  $\sim 38$  MeV/c $^2$*   
1283 *in the  $\gamma\gamma$  invariant mass spectra in pC, dC, and dCu collisions at  $p_{lab}$  of a*  
1284 *few GeV/c per nucleon*. 2023. Available from arXiv: 2311.18632 [hep-ex].
- 1285 23. THE MEG II COLLABORATION et al. *Search for the X17 particle in  $^7\text{Li}(p, e^+e^-)^8\text{Be}$*   
1286 *processes with the MEG II detector*. 2024. Available from arXiv: 2411.07994  
1287 [nucl-ex].
- 1288 24. HILKE, H J. Time Projection Chambers. *Rep. Prog. Phys.* 2010, vol. 73, no.  
1289 11, p. 116201. Available from DOI: {10.1088/0034-4885/73/11/116201}.
- 1290 25. NAVAS, S. et al. Review of particle physics. *Phys. Rev. D*. 2024, vol. 110,  
1291 no. 3, p. 030001. Available from DOI: 10.1103/PhysRevD.110.030001.
- 1292 26. ABED ABUD, Adam et al. A Gaseous Argon-Based Near Detector to En-  
1293 hance the Physics Capabilities of DUNE. 2022. Available from DOI: 10.  
1294 48550/arXiv.2203.06281.
- 1295 27. LOKEN, Stewart C. et al. Performance of the Signal Processing System for  
1296 the Time Projection Chamber. *IEEE Trans. on Nucl. Sci.* 1983, vol. 30, no.  
1297 1, pp. 162–166. Available from DOI: 10.1109/TNS.1983.4332243.
- 1298 28. ADAMOVÁ, D. et al. The CERES/NA45 radial drift Time Projection Cham-  
1299 ber. *Nucl. Instrum. Methods Phys. Res. Sect. A: Accel. Spectrom. Detect.*  
1300 *Assoc. Equip.* 2008, vol. 593, no. 3, pp. 203–231. ISSN 0168-9002. Available  
1301 from DOI: 10.1016/j.nima.2008.04.056.

- 1302 29. HILDÉN, T. et al. Optical quality assurance of GEM foils. *Nucl. Instrum.*  
1303 *Methods Phys. Res. Sect. A: Accel. Spectrom. Detect. Assoc. Equip.* 2015,  
1304 vol. 770, pp. 113–122. ISSN 0168-9002. Available from DOI: 10.1016/j.nima.2014.10.015.
- 1305
- 1306 30. AHMED, Misbah Uddin. *Simulation of the electron and ion movement through a 4-GEM stack.* 2021. Institut für Kernphysik.
- 1307
- 1308 31. MARMELAD. *3D interpolation2.svg.* 2025. Available also from: [https://commons.wikimedia.org/wiki/File:3D\\_interpolation2.svg](https://commons.wikimedia.org/wiki/File:3D_interpolation2.svg). Licensed  
1309 under CC BY-SA 3.0 (<https://creativecommons.org/licenses/by-sa/3.0/legalcode>). Accessed: 9-April-2025.
- 1310
- 1311
- 1312 32. CMGLEE. *Trilinear interpolation visualisation.* 2025. Available also from:  
1313 [https://commons.wikimedia.org/wiki/File:Trilinear\\_interpolation\\_visualisation.svg](https://commons.wikimedia.org/wiki/File:Trilinear_interpolation_visualisation.svg). Licensed under CC BY-SA 3.0 (<https://creativecommons.org/licenses/by-sa/3.0/legalcode>). Accessed: 26-March-2025.
- 1314
- 1315
- 1316 33. SMIRNOV, I.B. Modeling of ionization produced by fast charged particles in  
1317 gases. *Nucl. Instrum. Methods Phys. Res. Sect. A: Accel. Spectrom. Detect.*  
1318 *Assoc. Equip.* 2005, vol. 554, no. 1, pp. 474–493. ISSN 0168-9002. Available  
1319 from DOI: <https://doi.org/10.1016/j.nima.2005.08.064>.

1320 **Acknowledgments:** Computational resources were provided by the e-INFRA  
1321 CZ project (ID:90254), supported by the Ministry of Education, Youth and Sports  
1322 of the Czech Republic. **Figures that were drawn with GeoGebra. Maybe grant?**

# 1323 List of Figures

1324 0.1	The ATOMKI anomalous IPC measured for different nuclei. . . . .	5
1325 0.2	Results from the Hanoi spectrometer – angular $e^+e^-$ pair correlations measured in the ${}^7\text{Li}(p, e^+e^-){}^8\text{Be}$ reaction at $E_p = 1225$ keV [21]. . . . .	6
1326 0.3	Results from the MEG II experiments – angular correlation of $e^+e^-$ pairs with $E_{\text{sum}} \in [16, 20]$ MeV measured in the ${}^7\text{Li}(p, e^+e^-){}^8\text{Be}$ reaction with proton beam energies 500 and 1080 keV. The 500 keV dataset is fitted with Monte Carlo of both the IPC deexcitation and the EPC produced by gammas [23]. . . . .	7
1327 0.4	Schematics of the detector at the Van der Graaff facility at IEAP CTU (ref). . . . .	7
1333 1.1	Particle identification in the PEP-4 TPC at SLAC based on the energy loss per distance $\frac{dE}{dx}$ in the 80:20 Ar:CH <sub>4</sub> filling at 8.5 atm pressure [26]. <b>The reference doesn't point to the original PEP-4 article because this adapted version of the original picture that they used in the DUNE article looks better.</b> . . . . .	9
1334 1.2	Schematic view of the PEP-4 TPC [27]. A charged particle produced in a collision in the beam pipe creates a spiral ionization track in the magnetic field. The central cathode then accelerates ionization electrons towards the endcap anode wires where they are multiplied and read out. . . . .	12
1335 1.3	Gas Electron Multiplier (GEM). . . . .	14
1336 1.4	Garfield simulation of an avalanche in a GEM hole [30]. An incoming electron (orange) is accelerated in the strong electric field of the GEM and causes further ionization multiplying the number of free electrons (orange). Most of the produced cations (red) are captured by the GEM cathode. . . . .	14
1337 1.5	MICRO-MEsh GAseous Structure (Micromegas) [25]. . . . .	15
1338 1.6	Schematics of the first sector OFTPC with detector space coordinates. . . . .	17
1339 1.7	Pad layout of the OFTPC and its parameters. Pads 102, 124 and 127 are irregular, the rest has the same dimensions. . . . .	18
1340 1.8	Magnetic field simulation results. The OFTPC volume and the vacuum tube are marked with black lines, the magnets are marked with red lines. <b>The coordinates of the magnets from the CAD drawing seem to be 9/10 of the ones from the magnetic simulation (confirm and fix).</b> . . . . .	19
1341 1.9	Visualization of trilinear interpolation as a composition of linear interpolations (inspired by [31]). We want to interpolate the value in the red point C. First we interpolate between the four pairs of blue points sharing the last two indices along the x-axis (Eq. 1.15), then between the two pairs of the resulting green points along the y-axis (Eq. 1.16) and finally between the two resulting orange points along the z-axis to get the final red value (Eq. 1.17). . . . .	20

1366	1.10 Geometric interpretation of trilinear interpolation as expressed in Equation 1.19. The colored dots represent the values in given points and the colored boxes represent the volume in the opposite corner by which the corresponding values are multiplied. The black dot represents the interpolated value which is multiplied by the entire volume [32]. . . . .	21
1372	2.1 Comparison of drift lines for two different gas mixtures 90:10 and 70:30 Ar:CO <sub>2</sub> . The electron track is marked in black, the drift lines of the ionization electrons are marked in orange. In this example, we assume a larger OFTPC volume with readout at $z = 8$ cm. . . . .	24
1376	2.2 A visualization of a set of tracks from the grid-like testing sample with the same kinetic energy. . . . .	25
1378	2.3 A comparison of the HEED track from the microscopic simulation in Section 2.1.1 with a Runge-Kutta track with the same initial parameters and $\tau_{\text{step}} = 0.1$ ps (reducing the step further doesn't make a visible difference). In the view of the tracks on the left, the distance of the HEED ionization electrons from the RK4 track is exaggerated 1000 $\times$ . On the right, the dependence of the HEED electrons residuals (i.e., their shortest distance to the RK4 track) on their $z$ -coordinate is shown. <b>The images look the same even for 100,000x smaller step, so the residuals are a result of something that HEED does (maybe a different interpolation technique for the magnetic field? the pattern looks similar for two different tracks so it can't be scattering).</b> . . . . .	27
1390	3.1 Linear fit of the drift time $t$ dependence on the distance to the readout $d_r = 8$ cm – $z$ for the ionization electrons in 90:10 (left) and 70:30 (right) Ar:CO <sub>2</sub> gas composition. Only electrons inside the TPC (red) are fitted. The parameters are $v_d = 3.39$ cm/ $\mu$ s, $d_0 = -0.41$ cm for 90:10, and $v_d = 0.939$ cm/ $\mu$ s, $d_0 = -0.11$ cm for 70:30 Ar:CO <sub>2</sub> . . . . .	29
1396	3.2 Reconstruction (black) of the starting position of ionization elec- trons (red) using parameters obtained from the fit (Fig. 3.1). Two gas compositions 90:10 (left) and 70:30 Ar:CO <sub>2</sub> (right) are compared. . . . .	30
1399	3.3 Comparison of residuals (i.e., the distance from the reconstructed point to the simulated ionization electron starting point) depen- dence on $x$ for two gas mixtures 90:10 (red) and 70:30 Ar:CO <sub>2</sub> (blue). . . . .	30
1403	3.4 A 3D visualization of the mapping of means $\overline{\mathcal{M}}$ for the 90:10 Ar:CO <sub>2</sub> gas. A regular grid $\mathbb{G}$ with $l = 1$ cm in the detector space is mapped to an irregular grid $\mathbb{G}^{-1} \equiv \overline{\mathcal{M}}(\mathbb{G})$ in the readout space. . . . .	31
1406	3.5 A test of the 90:10 Ar:CO <sub>2</sub> map simulation with spacing $l = 1.5$ cm. The resulting drift lines of evenly spaced electrons are displayed in orange. . . . .	32
1409	3.6 Dependence of the drift times of the simulated map $\overline{\mathcal{M}}$ on the $z$ -coordinate. Two gas mixtures 90:10 (left) and 70:30 Ar:CO <sub>2</sub> (right) are compared. The spread is caused by varying Lorentz angles. . . . .	33

1413	3.7	The $x't$ projection of the $\mathcal{M}(\mathbb{G}_{y=0})$ mapping of a part of the regular grid $\mathbb{G}$ . The means $\overline{\mathcal{M}}(\mathbb{G}_{y=0})$ are marked with red crosses, and the diffusion error is denoted by black 95% confidence error ellipses computed from the diagonalized covariance matrices $\mathcal{M}_\Sigma(\mathbb{G}_{y=0})$ . Two gas mixtures 90:10 (left) and 70:30 Ar:CO <sub>2</sub> (right) are compared. The first mixture shows differences of $t$ for electrons with same initial $z$ but different initial $x$ . For the second mixture, these differences are negligible in comparison with the diffusion. . . . .	33
1421	3.8	The regular grid $\mathbb{G}$ projected by the mapping $\overline{\mathcal{M}}$ from the detector space onto the $x'y'$ plane ( $t$ is not plotted). Layers with lower $z$ -coordinate (i.e., further away from the readout) are displayed with darker colors. The OFTPC volume is marked with black lines. Two gas mixtures 90:10 (left) and 70:30 Ar:CO <sub>2</sub> (right) are compared. . . . .	34
1427	3.9	The $\mathcal{M}(\mathbb{G}_{-8})$ mapping of the bottom ( $z = -8$ cm) layer $\mathbb{G}_{-8}$ of the regular grid $\mathbb{G} \subset \mathcal{D}$ . It includes both the mapping of means $\overline{\mathcal{M}}$ and of covariances $\mathcal{M}_\Sigma$ . Individual electrons from the map simulation are marked with red dots. Two gas mixtures 90:10 (left) and 70:30 Ar:CO <sub>2</sub> (right) are compared. . . . .	34
1432	3.10	The readout coordinate $x'$ for points on the grid $\mathbb{G}_{y=0}$ plotted against their initial coordinate $z$ . The means are marked with red crosses, the diffusion in $x'$ is denoted by standard error bars. Two gas mixtures 90:10 (left) and 70:30 Ar:CO <sub>2</sub> (right) are compared. . . . .	35
1436	3.11	Example reconstruction with the map. <b>Swap for better image, correct coordinates.</b> . . . . .	36
1438	3.12	Selection of the points for interpolation. <b>Create better images; use the explanation interpolation vs. extrapolation strange property. Solution 2 probably does not make much sense.</b> . . . . .	39
1441	4.1	Example of a fitted reconstructed track. <b>Swap for better image.</b> . . . . .	41
1442	4.2	First attempt at a track reconstruction using only the drift velocity. Spline energy reconstruction attempt. <b>Swap for better image(s) – subfigure environment, correct coordinates.</b> . . . . .	43
1445	4.3	First attempt at a track reconstruction using only the drift velocity. Circle and Lines Fit in 2D. <b>Swap for better image, correct coordinates. Bias should be described in the previous chapter, not here.</b> . . . . .	45
1449	4.4	Visualization of the 3D geometry of the Circle and Lines Fit and its parameters. . . . .	46
1451	4.5	Demonstration of the convexity of the distance function $d(\alpha)$ for a circular track (see Equation 4.29). . . . .	49

- 1453    4.6 An example track (red) with a polygonal chain approximation  
 1454    (green, representing a RK4 simulation). The distance of the point  $\mathbf{P}$   
 1455    from the chain is found using a binary search among the distances  
 1456    to the vertices  $d_{\mathbf{P}}(\tau_i)$  (blue) and subsequently calculating the dis-  
 1457    tance to segments neighboring the found vertex (thus finding the  
 1458    minimum of the function  $d'_{\mathbf{P}}(\tau)$ , function  $d_{\mathbf{P}}(\tau)$  for the actual track  
 1459    is showed for reference). This approach works if the condition 4.28  
 1460    is satisfied, which is not the case for a point from the green area  
 1461    bordered by the normals at endpoints and the evolute of the track  
 1462    (orange). . . . .  
 1463    4.7 An exclusion area (green) of a track (red) bordered by its evolute  
 1464    and the normals at endpoints (orange), where the assumption 4.28  
 1465    is violated. Unlike the track in Fig. 4.6, this track has a minimal  
 1466    curvature point in the middle, corresponding to the cusp on its  
 1467    evolute. . . . .

50

51

# **List of Tables**

<sup>1468</sup>	3.1 Comparison of parameters of two map simulations. . . . .	32
-----------------	--	----

# <sup>1470</sup> List of Abbreviations

- <sup>1471</sup> **GEM** Gas Electron Multiplier
- <sup>1472</sup> **HEED** High Energy Electro-Dynamics
- <sup>1473</sup> **IEAP CTU** Institute of Experimental and Applied Physics, Czech Technical  
<sup>1474</sup> University in Prague
- <sup>1475</sup> **IPC** Internal Pair Creation
- <sup>1476</sup> **EPC** External Pair Creation
- <sup>1477</sup> **LArTPC** Liquid Argon TPC
- <sup>1478</sup> **Micromegas** MICRO-MEsh GAseous Structure
- <sup>1479</sup> **MPGD** Micro-Pattern Gaseous Detector
- <sup>1480</sup> **MWPC** Multi-Wire Proportional Chamber
- <sup>1481</sup> **OFTPC** Orthogonal Fields TPC
- <sup>1482</sup> **PCB** Printed Circuit Board
- <sup>1483</sup> **RK4** Runge-Kutta 4th order
- <sup>1484</sup> **RPC** Resistive Plate Chamber
- <sup>1485</sup> **RPWELL** Resistive Plate WELL
- <sup>1486</sup> **THGEM** THick GEM
- <sup>1487</sup> **ToA** time-of-arrival
- <sup>1488</sup> **ToT** time-over-threshold
- <sup>1489</sup> **TPC** Time Projection Chamber
- <sup>1490</sup> **TPX3** Timepix3
- <sup>1491</sup>  **$\mu$ -PIC** Micro-Pixel Gas Chamber
- <sup>1492</sup>  **$\mu$ -RWELL** Micro-RWELL